2022-05-01

Exploring Tunable Magnetization And High-Temperature Ferromagnetism In Ternary Transition Metal-Based Chalcogenides

Hector Iturriaga
The University of Texas at El Paso

EXPLORING TUNABLE MAGNETIZATION AND HIGH-TEMPERATURE FERROMAGNETISM IN TERNARY TRANSITION METAL-BASED CHALCOGENIDES

HECTOR ITURRIAGA

Master's Program in Physics

APPROVED:

Srinivasa Rao Singamaneni, Ph.D., Chair

Chunqiang Li, Ph.D.

Sreeprasad T. Sreenivasan, Ph.D.

Stephen L. Crites, Jr., Ph.D.
Dean of the Graduate School

DEDICATION

To everyone who helped me along the way

EXPLORING TUNABLE MAGNETIZATION AND HIGH-TEMPERATURE FERROMAGNETISM IN TERNARY TRANSITION METAL-BASED CHALCOGENIDES

by

HECTOR ITURRIAGA, B.Sc.

THESIS

Presented to the Faculty of the Graduate School of

The University of Texas at El Paso

in Partial Fulfillment

of the Requirements

for the Degree of

MASTER OF SCIENCE

Department of Physics

THE UNIVERSITY OF TEXAS AT EL PASO

May 2022

ACKNOWLEDGEMENTS

I cannot underscore enough the importance of the many collaborators that have contributed to the completion of this work. I want to thank Drs. Yu Liu and Cedomir Petrovic for providing our group with the crystals on which much of our work focuses. I extend my gratitude to Dr. Lin Shao for conducting the proton irradiation on several of the compounds. Dr. Martin Kirk and his student, Ju Chen, were also extremely critical in this work. I am extremely grateful for their help and cooperation with the extensive magnetometry measurements they completed on our behalf at UNM. In addition, I'd also like to thank them and Dr. Jing Yang at UNM for their help and guidance regarding EPR measurements. I must also acknowledge Drs. Ikenna Nlebedim, and Kinjal Gandha for their guidance in the preliminary magnetometry of the irradiated compounds at Ames Laboratory. Aside from this, I want to highlight the importance of their mentorship and support throughout the years. Also invaluable to this work are Dr. Sreeprasad Sreenivasan and his student, Mohamed Sanad, for the fabrication of the two-electrode setup that facilitated the successful intercalation of samples and preliminary Raman spectroscopy measurements. For their help with temperature dependent Raman spectroscopy measurements, I must thank Dr. Angela Hight-Walker and Dr. Thuc Mai at NIST and their guidance. Furthermore, I thank Dr. Elton Santos, and Mathis Agustin for the support they provided on the theory side of everything.

To all the lab mates who have come and gone, I thank you for your companionship and support throughout our time together, however brief it may have been. In particular, I want to thank Rubyann Olmos and Luis Martinez, who started off as mentors to me, but have since become close colleagues and friends to me. As we step into new chapters of our careers, I'm grateful for what you've taught me and what we've come to learn together. To my friends and family, thank you for your support and encouragement outside of the lab.

Finally, I extend the largest part of my gratitude to my research advisor, Dr. Srinivasa Rao Singamaneni, who has supported my professional and academic career throughout such a pivotal time in my journey. Many of the professional opportunities I've been honored with would not have come to fruition without his support and guidance.

This material is based upon work supported by the National Science Foundation Graduate Research Fellowship under Grant No. 184874. SRS acknowledges support from NSF-MRI (Award No. 2018067) and NSF-DMR (Award No. 2105109). Additional support was provided by the NSF—Louis Stokes Alliance for Minority Participation (LSAMP) program (Award number: 1826745) and The University of Texas at El Paso (UTEP) Nuclear Regulatory Commission, award number 31310018M0019. Work at the Ames Laboratory was supported by the U.S. Department of Energy Office of Science—Louis Stokes Alliance for Minority Participation (LSAMP) program under its contract with Iowa State University, Contract No. DE-AC02-07CH11358.

ABSTRACT

The discovery of long-range magnetic ordering in ultrathin transition metal-based compounds shows great promise for the development of nanoscale memory and spintronic devices. Composed of cost-effective materials and boasting from strong chemical and thermal stability at low dimensions, van der Waals (vdW) ternary transition metal chalcogenide magnets like $CrSiTe_3$ (CST), $Fe_{2.7}GeTe_2$ (FGT), and $Mn_3Si_2Te_6$ (MST), provide not only possible energy solutions, but also a broad platform to explore the versatile magnetic character of this family of compounds. Although they have great potential, it has been found that their long-range magnetic ordering exists at temperatures far too low (the highest of these is for FGT, $T_C \sim 153$ K) to be used in practical applications. Therefore, there is a big push toward finding ways of improving their magnetic characteristics at room temperature. Understanding and targeting the inner mechanisms governing the magnetism in these systems is a crucial step towards creating more effective functional devices. To these ends, we have employed non-destructive proton irradiation to enhance the magnetic properties of CST and MST and explored its effects on the bulk magnetization and Curie temperature as a function of magnetic field and irradiation fluence up to 10^{18} protons per unit area (H^+/cm^2). Further analysis on the magnetocrystalline anisotropy and magnetic entropy of the proton irradiated systems also serve to uncover the effects of mechanical perturbations on their intrinsic exchange mechanisms, which may prove useful for improving the functionality of these compounds as they are scaled to the two-dimensional level.

The versatility of vdW systems is highlighted through the proton irradiation studies; thus, we move to explore a more invasive method of enhancement involving the electrochemical intercalation of organic tetrabutylammonium cations into the vdW gap of our compounds. We again explore the changes in the magnetization, magnetic anisotropy, and Curie temperature

resulting from this process and find novel high-temperature features. Most notably, we confirm the presence of ferromagnetism up to 350 K in intercalated FGT. Spectroscopy data eliminate the possibility of crystal structure damage as the source of this effect; therefore, we look towards temperature-dependent Raman spectroscopy, spin-phonon coupling, and theoretical calculations for an explanation. From these experiments, we explore the possibility of a charge transfer effect and the role of modifications to the electronic structure of vdW magnets as an explanation to the observed changes. This study explores the different interactions within FGT and the processing methods that may lead to achieving robust room-temperature magnetism for applications.

TABLE OF CONTENTS

LIST OF TABLES

LIST OF FIGURES

PART I: TUNABLE MAGNETIZATION OF LAYERED VAN DER WAALS CHALCOGENIDES VIA PROTON IRRADIATION

CHAPTER 1: BACKGROUND AND MOTIVATION

The discovery of long-range magnetic ordering in atomically thin materials catapulted the van der Waals (vdW) family of compounds into an unprecedented popularity. [1,2] They are characterized by strong intralayer bonds but relatively weak vdW interlayer bonds, which allow for quasi-two-dimensional magnetic character even in the bulk. [2] Indeed, pioneering transition metal-based vdW magnets such as CrI_3 and $Cr_2Ge_2Te_6$ have been successfully studied at the single-layer limit, displaying novel and exciting long-range magnetic ordering at this 2-dimensional level. This offers hope for the creation of ultrathin magnetic data storage devices, spintronic applications, and other cost-effective magnetic devices. [2–5] In addition, with the current trend of space exploration, it is beneficial to investigate the behavior of vdW materials under the effects of proton irradiation. In space, where proton irradiation is abundant, bombardment with particles can quickly evolve into destructive damage. The robust intralayer properties of vdW compounds make them excellent candidates for studying the limits of proton irradiation on functional materials.

Particularly, though not exclusively, in the case of ternary transition metal-based vdW chalcogenides such as $Fe_{2.7}GeTe_2$ (FGT) and $Mn_3Si_2Te_6$ (MST), it has been found that proton irradiation serves as a non-destructive tool for controlling the magnetic properties of these compounds. [6–9] These compounds owe their enhanced magnetization after irradiation to their strong intralayer bonds, robust magnetic character, and sensitivity to external perturbations. In this study, we seek to explore the effects of non-destructive proton irradiation on the sister compound $CrSiTe_3$ (CST). In atomically thin samples, the realization of ferromagnetism was previously thought to be impossible as the Mermin-Wagner theorem suggested that thermal fluctuations would destroy any long-range magnetic ordering in the system. However, advancements in the field revealed that the magnetic anisotropy stabilizes the magnetic ordering of atomically thin vdW samples, proving that the magnetism of CST is stable even at the atomic level. [10] Unfortunately,

it is found that the Curie temperature (T_C) of CST is approximately 36 K, which makes it unsuitable for consumer applications. Regardless, techniques such as proton irradiation may prove to be useful in fulfilling the excellent potential of CST as a building block of functional magnetic materials. [11] Thus, we investigate the evolution of the T_C, saturation magnetization, and magnetocrystalline anisotropy in CST crystals irradiated at several fluences up to 1 x 10^{18} H^+/cm^2.

CHAPTER 2: EXPERIMENTAL METHODS

2.1 Synthesis and Irradiation

The synthesis of $CrSiTe_3$ was conducted as previously reported with the self-flux method starting with Cr powder and Si and Te pieces. [12] The process of CST and MST growth is outlined by Liu and Petrovic and resulted in mm-sized bulk single crystals. The crystals were then irradiated with a 2 MeV proton beam in 1.7 MV Tandetron Accelerator following closely the procedure outlined in our previous irradiation work. [6,7] The energy of the beam is kept low enough to avoid damage to the crystal. In addition, the weak beam current of 100 nA, beam spot size of 6mm x 6mm rastered over an area of 1.2 cm x 1.2 cm, and magnetic bending filters ensure lateral beam uniformity, minimal heating, and eliminate carbon contamination. The projected implantation depth is approximately 35 microns according to the damage profile, which shows a uniform distribution of H from the surface down to approximately 30 microns from the surface, at which point there is a noticeable increase. The fluences selected for this study are 0 (referred to as pristine in this work), 1 x 10^{15}, 5 x 10^{15}, 1 x 10^{16}, 5 x 10^{16}, and 1 x 10^{18} H^+/cm^2.

2.2 Magnetic and Thermal Characterization

The magnetic properties of the crystals were characterized using a Quantum Design Magnetic Property Measurement System 3 (MPMS 3) Superconducting QUantum Interference Devices/Vibrating Sample Magnetometer (SQUID/VSM) hybrid system. DC moment data were extracted using the VSM option throughout all temperature and field ranges. The measurements were conducted in a temperature range of 2 K – 300 K and magnetic fields up to 30 kOe in both polarities. Samples were loaded separately into the instrument, wrapping them first in Teflon tape to avoid contamination from sample holders or from contact with the instrument chamber. In the case of anisotropic magnetic moment, we use both quartz and brass holders which allow for in-plane (where the crystallographic ab-plane is parallel to the applied field) and out-of-plane (where

the c-axis is parallel to the applied field) measurements. Contributions to the magnetic moment from the sample holders are corrected by the MPMS 3 MultiVu software.

Heat capacity measurements were completed using a Quantum Design VersaLab system in a temperature range of 50 K – 300 K. The samples were affixed to a calibrated calorimeter puck by vacuum suction for stabilization and Apiezon H grease for adhesion. The addenda contribution was measured beforehand to allow for facile extraction of the sample heat capacity.

2.3 Electron Paramagnetic Resonance Spectroscopy

Low temperature X-band electron paramagnetic resonance (EPR) spectroscopy measurements were conducted for each sample. Each sample was wrapped with Teflon and mounted onto a sample holder such that the c-axis was parallel to the applied magnetic field. The samples are taken to a specified temperature point, allowed to reach thermal equilibrium, and then the magnetic field is scanned from 0 G to 7000 G. To avoid the effects of remanent magnetization between temperature points, the magnetic field was removed, the sample was warmed above its Curie temperature, and finally cooled down to the next temperature point. Measurements were done at select temperatures between 10 K and 77 K.

CHAPTER 3: MAGNETIC PROPERTIES AFTER PROTON IRRADIATION

3.1 TEMPERATURE-DEPENDENT MAGNETIZATION

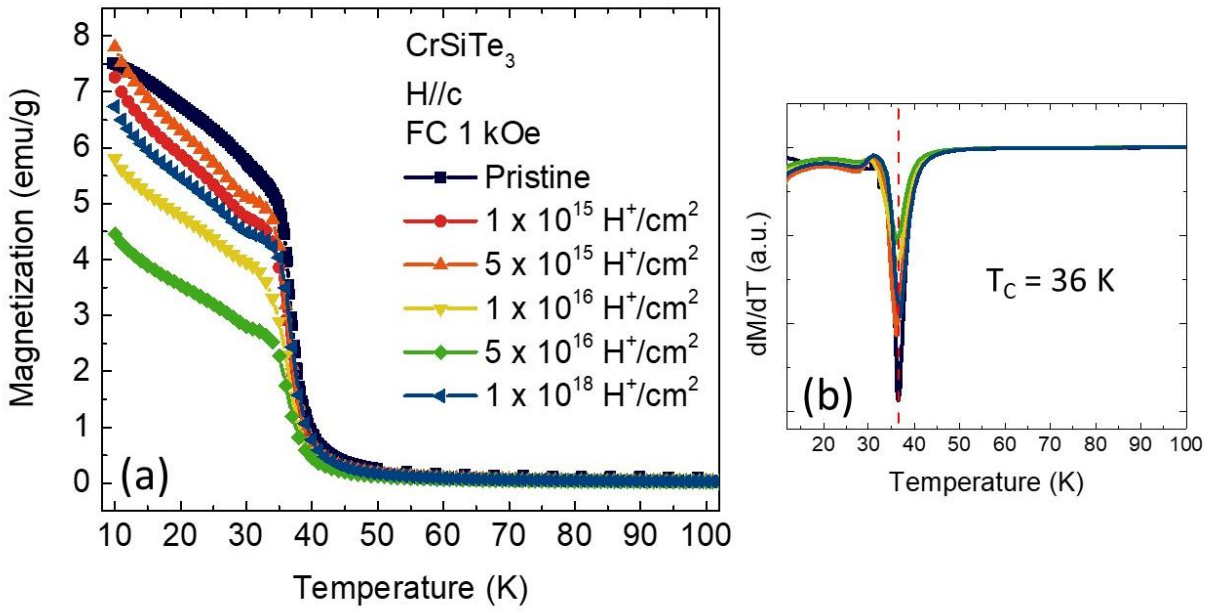

Figure 3.1: Magnetization vs. temperature (a) and dM/dT vs. temperature (b) shown as a function of fluence showing the ferromagnetic to paramagnetic transition at T_c = 36 K for all samples

Figure 3.1a shows a plot of magnetization vs. temperature at all fluences. These measurements were collected along the out-of-plane (H//c) direction with a cooling field of 1 kOe. These field cooled (FC) measurements were conducted by cooling the sample from room temperature down to 10 K under an applied magnetic field. The sample is allowed to reach thermal equilibrium before the magnetic field is set to 500 Oe and the temperature is incremented back to 300 K. For a better visualization of the ferromagnetic phase of CST, only the range from 10 K – 100 K is shown as the samples are paramagnetic beyond 50 K. In figure, we present a sharp transition for all samples regardless of proton fluence. Estimation of the Curie temperature (T_C) via the first derivative of the magnetization with respect to the temperature (figure 3.1b) returns a value of approximately 36 K, which agrees well with literature reports. [12–14] In addition, the low temperature behavior shows that there is a clear change in magnetization after irradiation. Unexpectedly, the magnetization of the 5 x 10^{15} H^+/cm^2 fluence (orange, upright triangles) slightly exceeds the magnetization of the pristine sample at 10 K, before rapidly dropping below the

pristine magnetization at 12 K. Aside from that, for all other fluences there is a clear decrease in the magnetization.

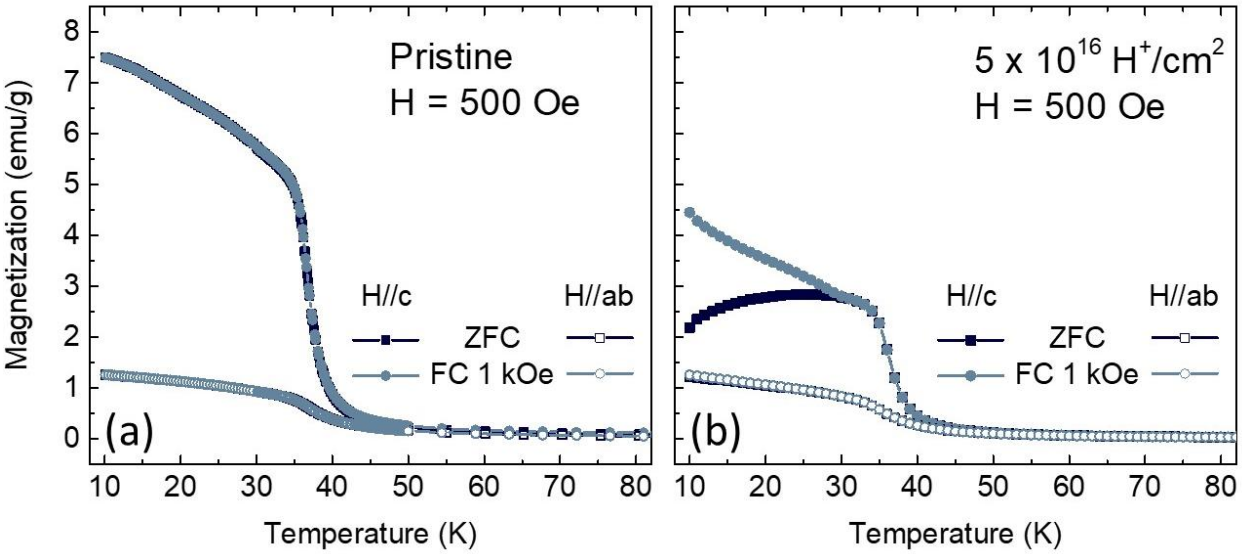

Figure 3.2: Anisotropic magnetization vs. temperature for both pristine (a) and irradiated (b) CST as a function of cooling field

Particularly, at 10 K, the sample irradiated with 5 x 10^{16} H^+/cm^2 (figure 3.1a, green, rhombus) displays a magnetization of 4.5 emu/g, a 40% decrease from the pristine magnetization of 7.5 emu/g. This fluence shows the most dramatic decrease, hence the comparison between it (figure 3.2b) and the pristine (figure 3.2a) magnetization will be emphasized for the following discussion of anisotropic temperature-dependent measurements. These measurements were also completed along the in-plane direction (H//ab) to gather information about the magnetocrystalline of the samples. Shown in Figure 3.2 is a comparison of the H//c (solid symbols) and H//ab (open symbols) magnetization vs. temperature curves for both FC (cyan symbols) and ZFC (navy blue symbols) measurements. ZFC measurements were completed by cooling the sample without a magnetic field. As expected, the magnetization is higher in the H//c direction, as this is the magnetic easy axis of CST and serves as evidence of strong perpendicular magnetocrystalline anisotropy in the system. [10,12–16] This remains true for the irradiated samples, providing evidence that the easy axis remains stable despite a decrease in magnetization. The H//c measurement for the irradiated sample shows a large bifurcation between the FC and ZFC curves

at low temperatures. This feature is not present in the pristine magnetization, which could be a first indication of alterations to the magnetic anisotropy of irradiated CST. In addition, the H//ab magnetization is similar in both samples. However, this may be because the applied field is too small to accurately detect any anisotropic effects in this direction.

3.2 MAGNETIC FIELD-DEPENDENT MAGNETIZATION

Figure 3 shows the isothermal magnetic field-dependent magnetization of all fluences at several temperatures below (figures 3.3a, 3.3b, 3.3c, 3.3d) and above (figures 3.3e, 3.3f) $T_C \sim 36$ K. Samples were cooled from room temperature to the target measurement temperature and allowed to reach equilibrium in the absence of a magnetic field. For these measurements, the samples were subjected to a 5-quadrant field sweep, where the field is ramped up from 0 Oe, up to the maximum field of +30 kOe, and then incremented back through 0 Oe and down to -30 kOe, before finally increasing the field back to its maximum value. For isotherms below T_C, the system is warmed to its paramagnetic state under no magnetic field upon completing the measurement and cooled to the next target temperature to avoid remanence effects. The measurements are done in both the H//c (figures 3.3a, 3.3c, 3.3d, solid symbols) and H//ab (figures 3.3b, 3.3d, 3.3f, open symbols) directions, which allows us to qualitatively and quantitatively analyze the magnetocrystalline anisotropy of irradiated CST. From these data, we also extract information about the effect proton irradiation has on the saturation magnetization and coercivity of CST.

Firstly, the hysteresis curves in figures 3.3a – 3.3d are clear proof of the ferromagnetic phase of CST at temperatures below T_C. Even after irradiation, all samples exhibit this typical ferromagnetic behavior. We also observe negligible coercivity across all fluences. In comparison to the H//ab data (figure 3.3b), the H//c saturation field along is far lower, further proving that CST maintains its perpendicular magnetic anisotropy with an H//c easy axis. Conversely, the H//ab magnetization saturates only at higher fields and shows a more gradual onset of saturation. The most obvious change that occurs after irradiation is a reduction in the saturation magnetization.

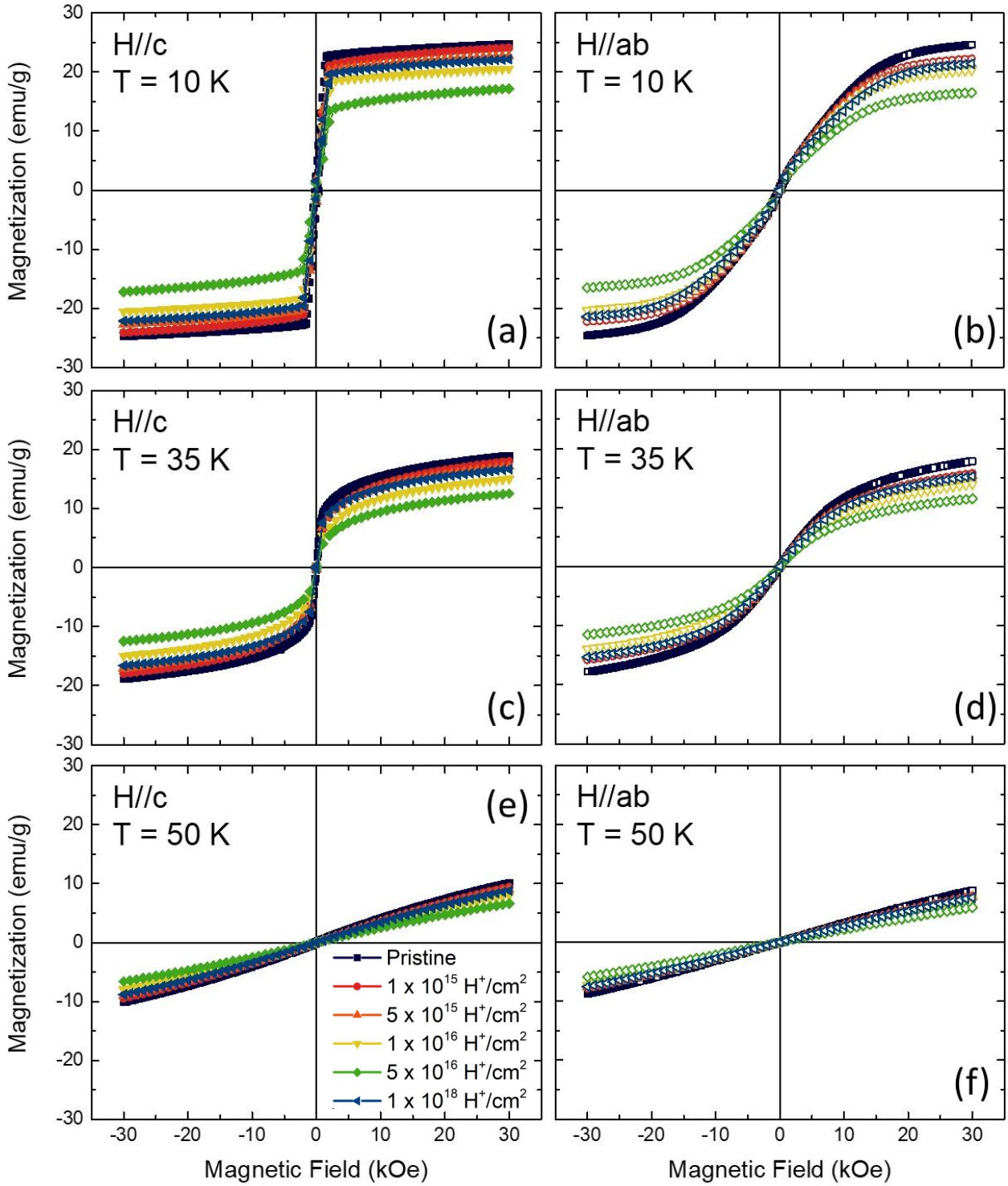

Figure 3.3: Magnetization vs. magnetic field as a function of fluence for H//c (a,c,e) and H//ab (b,d,f) at T = 10 K (a,b), 35 K (c,d), and 50 K (e,f)

Indeed, for the 5 x 10^{16} H^+/cm^2 fluence, the magnetization decreases by over 30%. This supports our initial observation in the temperature-dependent magnetization measurements. Figure 3.4 shows the saturation magnetization M_{sat} for all fluences as a function of temperature. The values of M_{sat} are taken from the H//c hysteresis curves at the maximum field. This plot reveals that the reduction in magnetization is not proportional to the number of protons per unit area. In fact, the median fluence of 1 x 10^{16} H^+/cm^2 (yellow, down triangle) shows lower values of magnetization than the highest fluence of 1 x 10^{18} H^+/cm^2 (blue, left triangle). Moreover, the fluence of 5 x 10^{16} H^+/cm^2 shows the lowest magnetization despite not being the highest fluence.

Indeed, there is a non-monotonic relationship between the proton fluence and the magnetization; hence, we cannot simply attribute the decrease in magnetization to a destruction of the crystal otherwise, 1 x 10^{18} H^+/cm^2 would exhibit the lowest magnetization. [6,7,17] Furthermore, the observed trend persists through the ferromagnetic to paramagnetic transition.

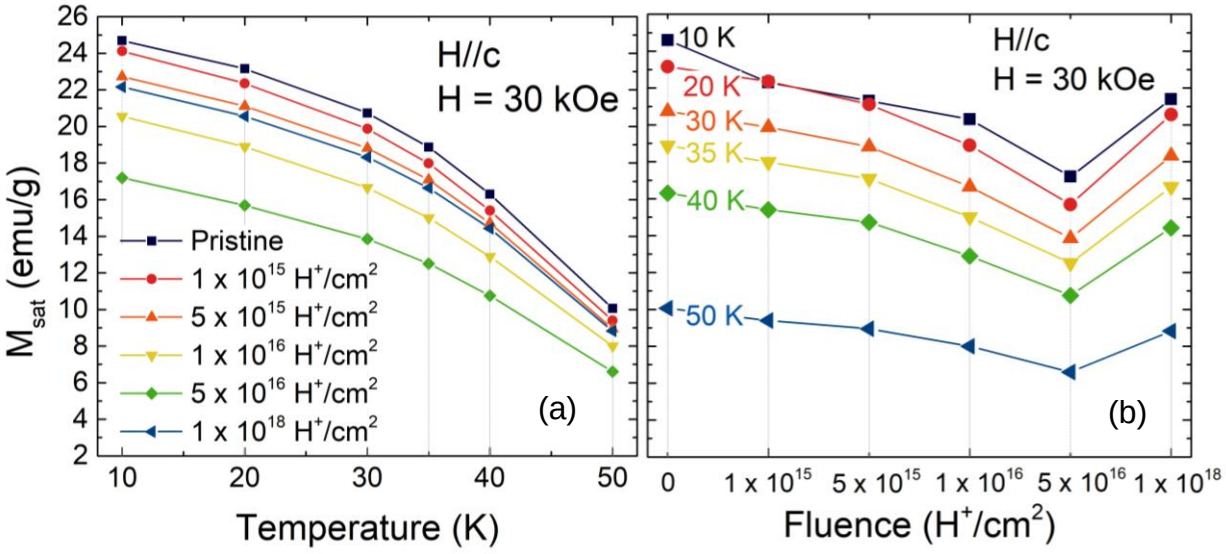

Figure 3.4: Saturation magnetization M_{sat} vs. temperature as a function of fluence (a) and M_{sat} vs. fluence at each temperature (b) showing non-monotonic relation between magnetization and proton irradiation

3.3 MAGNETIC ANISOTROPY

3.3.1 Motivation: Proton irradiated $Mn_3Si_2Te_6$

Previous reports on proton irradiated vdW $Mn_3Si_2Te_6$ demonstrated a similar non-linear relationship between fluence and magnetization with no change in T_C. In-depth analysis of the critical behavior of proton irradiation showed that the enhancement in magnetization was likely due to changes in the exchange mechanism. [6,17] We quantified the magnetic entropy through thermodynamic models of heat capacity. Heat capacity (C_p) data were taken for all irradiated samples from 50 K to 300 K in the absence of a magnetic field as shown in figure 3.5a. The kink at near 72 K can be attributed to the magnetic transition temperature. To investigate the magnetic entropy released across the magnetic transition, we employed the method of May et al. where C_p/T is plotted versus temperature (figure 3.5b) in the range of 60 K to 95 K to capture the magnetic transition. [18] Once this range is isolated, a linear background is subtracted as a substitute. The linear background subtraction serves two purposes: 1) it accounts for a lack of suitable phonon reference material and negligible electronic contribution and 2) intentionally overestimates the magnetic entropy in the system. Then, equation 1 is satisfied by taking the integral of this magnetic contribution to the heat capacity C_M over the isolated temperature range.

$$S_m = \int \left(\frac{C_M}{T}\right) dT \tag{1}$$

The saturation value of the entropy is taken as the maximum entropy released. Small variations are likely due to noise and differences in the linear background subtraction. Nonetheless, an analysis of these values reveals that the entropy released is considerably small and comparable across all fluences, even after a deliberate overestimation. To verify this, we also fitted the heat capacity data with a sum of two Einstein fits (figure 3.5c), derived from the Einstein model of heat capacity. [19] Due to a lack of low temperature data, appropriate reference for electron and phonon contributions, we refrained from including a Debye term. For this analysis, the high temperature data is fitted with model of the form:

$$C_E = \sum 3Rn_i \left(\frac{\theta_i}{T}\right)^2 \frac{e^{\theta_i/T}}{\left(e^{\theta_i/T} - 1\right)^2} \quad (2)$$

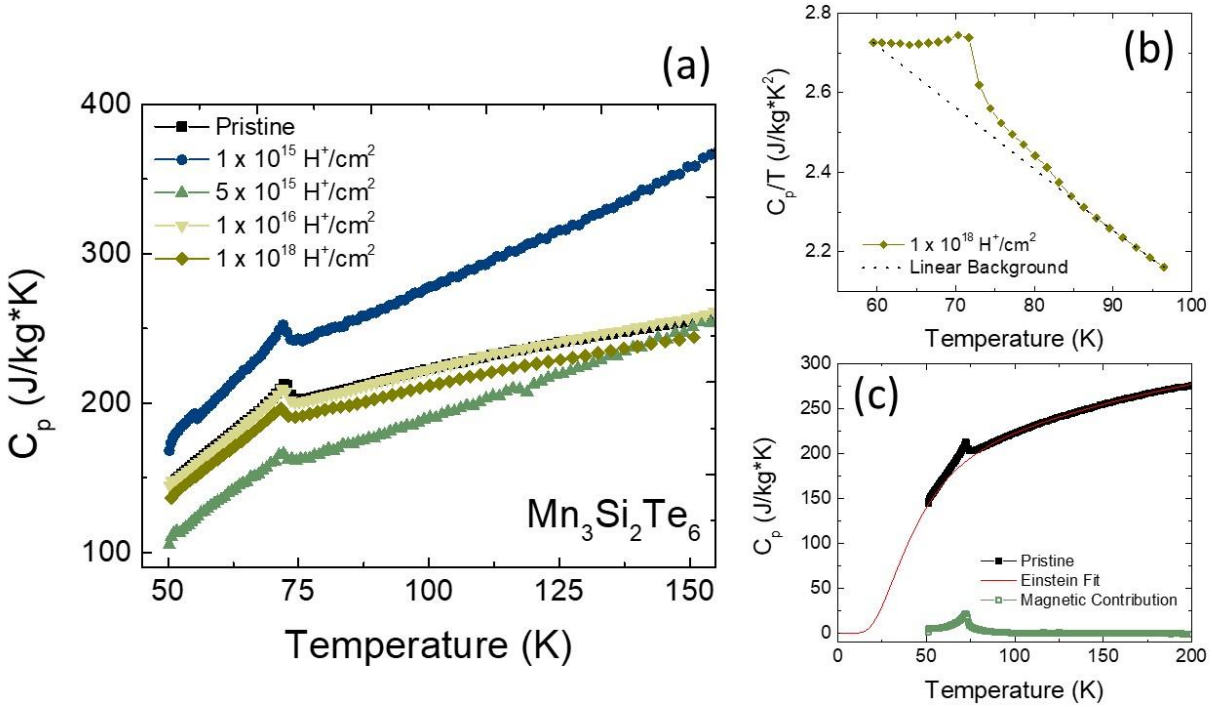

Figure 3.5: Heat capacity vs. temperature as a function of fluence (a). Examples of heat capacity models used: linear background subtraction (b) and Einstein model (c)

In this model, R is the specific gas constant of MST, n_i is a weight factor for each Einstein term, and θ_i serves as the Einstein temperature. The temperature range of each data set ranges slightly to acquire the best fit. With C_E acting as a simulated lattice contribution to the heat capacity, it is subtracted from the total heat capacity data and the magnetic contribution is isolated and treated as in the previous analysis. This method also provides an overestimation of the magnetic entropy, but reinforces the conclusions brought forth by the previous method: despite yielding larger values of S_m, they are still remarkably small. In effect, an even larger overestimation of the magnetic entropy still shows that only a small amount of magnetic entropy is released across the ferromagnetic to paramagnetic transition.

From equation 3, the magnetic entropy is analytically extracted and compared to the values acquired from the fits in table 3.1.

$$S_m = R \ln(2S + 1) \quad (3)$$

With S = 5/2 in MST, S_m = Rln(6) = .015 J/K which is the theoretical value of the total magnetic entropy in the system. Analysis on the heat capacity data demonstrates that the amount of released entropy experimentally detected is an order of magnitude smaller than what was expected. The percent columns in table 3.1 quantify the fraction of the total entropy that is released across the magnetic transition and show that not even deliberate overestimations come close to the expected value. Because of the frustrated short-range correlations in ferrimagnetic MST, it is likely that this behavior stems from a stable antiferromagnetic coupling between the present Mn1 and Mn2 sites. More importantly, since the values of released entropy are similar across all fluences, we believe that proton irradiation does not weaken the coupling between Mn sites. Otherwise, we would observe a larger amount of magnetic entropy being released as the temperature is raised above T_C. Thus, we also believe this could be evidence that there are modifications to the exchange mechanism of MST. Further details are outlined in our previous report. [17,20–25]

Table 3.1: Magnetic entropy S_m (J/K) released in ferromagnetic to paramagnetic transition.

Fluence (H^+/cm^2)	Linear Background	Percent	Einstein Model	Percent
0 (pristine)	.00199	13%	.0041	27%
1 x 10^{15}	.0024	16%	.0037	25%
5 x 10^{15}	.0016	11%	.0035	23%
1 x 10^{16}	.00187	12%	.0028	19%
1 x 10^{18}	.00187	12%	.0031	21%

In proton irradiated CST, we set out to correlate the changes in magnetization to any possible changes in the dominant exchange mechanism. In MST, this was indirectly probed through heat capacity and magnetic entropy analyses, which justify the need to consider the evolution of the magnetic exchange mechanisms within vdW systems as a function of proton irradiation.

3.3.2 Uniaxial anisotropy constant of proton irradiated $CrSiTe_3$

It is unlikely that damage to the CST crystals from increased proton irradiation is responsible for the observed reduction in magnetization because the trend between proton fluence and reduced magnetization is not proportional. Therefore, we examine the interatomic interaction of CST by investigating any changes in the magnetocrystalline anisotropy as a function of temperature and proton irradiation fluence. To do this, we extracted the effective anisotropy constant K_u using the Stoner-Wohlfarth model as shown in equation 4: [12,16,26–29]

$$\frac{2K_u}{M_{sat}} = \mu_0 H_{sat} \tag{4}$$

Here, M_{sat} is the saturation magnetization, H_{sat} is the anisotropy field, or saturation field along the hard axis, and μ_0 is the vacuum permeability. For clarity, the anisotropy field and the saturation magnetization are extracted from magnetic field vs. magnetization measurements done in the H//ab direction to capture to magnitude of magnetic field necessary to completely align the moments along an unpreferable direction. To estimate the onset of saturation along this direction, the second derivative of the first quadrant magnetization was taken with respect to the magnetic field and the field magnitude at the local minimum was taken as the saturation/anisotropy field. The multiplicative factor μ_0 is simply unity in cgs units. The values of H_{sat} (figure 3.6a) and K_u (figure 3.6b) for pristine CST acquired from this estimation agree well with the literature. [16] In figure 3.6b, K_u is shown for all fluences as a function of temperature below T_C. Only temperatures below T_c are selected as saturation is not achieved in the paramagnetic region. As expected, the overall values decrease with increasing temperature, but the fluence dependent behavior at each temperature mirrors that of the saturation magnetization with no simple linear relation.

The anisotropy constant for the sample irradiated with 5×10^{16} H^+/cm^2 is consistently lower than that of the other fluences across all temperatures. At first glance, it appears that this could be due to both a reduced H_{sat} and M_{sat}, but a closer inspection of the former reveals a deeper phenomenon related to the temperature dependence of the anisotropy. In fact, a temperature-

dependent H_{sat} is direct evidence of a temperature-dependent anisotropic behavior in CST. [28,29] Moreover, the anisotropy field shows a slight proportionality with the proton fluence. As shown in figure 3.6b, we observe that samples irradiated with more protons per unit area generally require a higher H//ab field to achieve saturation. This trend can be more clearly seen at 20 K (figure 3.6a, blue circles), and deviations at other temperatures are likely due to measurement error.

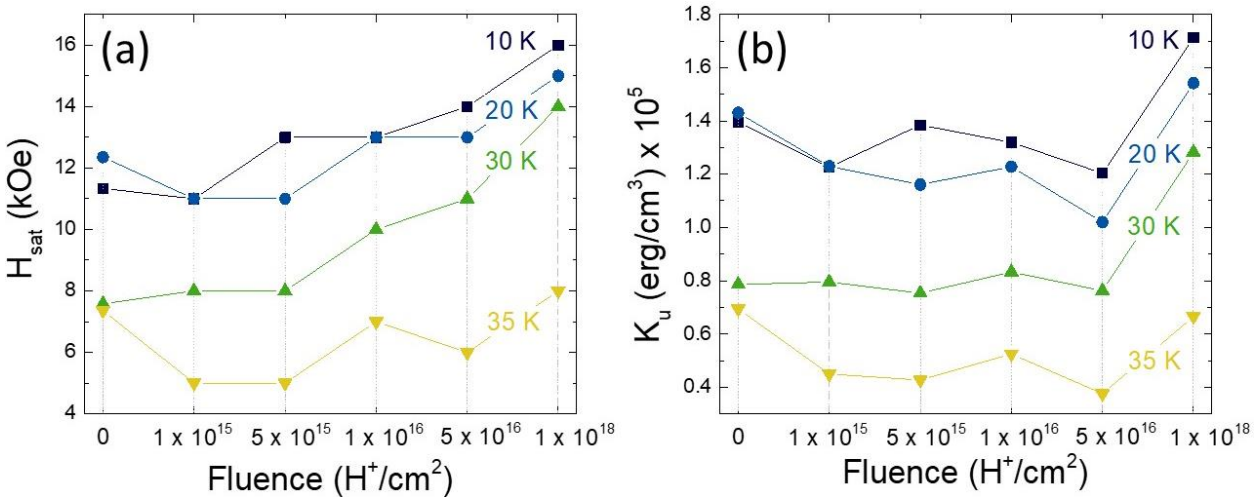

Figure 3.6: Anisotropy field H_{sat} (a) and uniaxial anisotropy constant K_u (b) vs. fluence as a function of temperature

Furthermore, a decrease in K_u is observed for all fluences as the temperature is increased. This phenomenon has been documented in other vdW compounds such as CrI_3 and Fe_3GeTe_2 and is attributed to fluctuating local spin clusters around a macroscopic magnetization vector. [12,28,29] Hence, a lower K_u in the irradiated samples could indicate an effect on their short-range interactions. In CST, the anisotropy is stabilized by two factors. The first is a slight distortion of Te octahedra along the c-axis and the second factor is the ligand Te p spin-orbit coupling through the dominant superexchange pathway in CST. [30–33] This Cr-Te-Cr superexchange is ferromagnetic in agreement with the Goodenough-Kanamori rules and dominates over the weak antiferromagnetic Cr^{3+} direct exchange, the non-negligible interlayer interactions, and the 2nd and 3rd nearest neighbor intralayer interactions. Therefore, changes in the anisotropy constant could be indirect evidence of modifications to the superexchange of proton irradiated CST, as it has been reported that the anisotropy of CST is sensitive to changes in the

superexchange and electronic repulsions. [32] In addition, though the 2nd and 3rd nearest neighbor interactions are a super-superexchange pathway across two Te ligand atoms (Cr-Te-Te-Cr), they present a suitable environment for antiferromagnetic couplings to exist in CST. [31,32] If enhanced through proton irradiation, this antiferromagnetic exchange could account for the reduction in magnetization despite an unchanged T_C. The dependence of the magnetic properties on proton fluence remains unclear; thus, more investigations on the exchange couplings of CST are needed.

CHAPTER 4: ELECTRON PARAMAGNETIC RESONANCE SPECTROSCOPY

The electron paramagnetic resonance (EPR) spectra for all samples were collected at temperatures ranging from 13 K to 77 K to capture the ferromagnetic to paramagnetic transition of CST. Shown in figure 4.1, the spectra as a function of proton fluence are shown at 13 K (figure 4.1a), 50 K (figure 4.1b), and 77 K (figure 4.2c). The temperatures represent the behavior of CST well into the ferromagnetic phase, then above T_C, and finally in the paramagnetic phase respectively. We observe the expected signal from the Cr^{3+} at all temperatures and all fluences with g-value ranging from 1.96109 - 1.9950 at 13 K depending on the fluence. [34,35] To extract the spectral parameters such as the linewidth, and center field, the data were fitted with a Lorentzian lineshape (dotted black line). In the spectrum of the pristine sample at 13 K, the Cr^{3+} signal dominates, but further inspection shows yet another positive resonance that is more readily observed in the spectra of the irradiated samples. This broad signal is centered at low fields and could not be completely captured by the magnetic field range of the spectrometer. Hence, further experiments are required to pinpoint its origin.

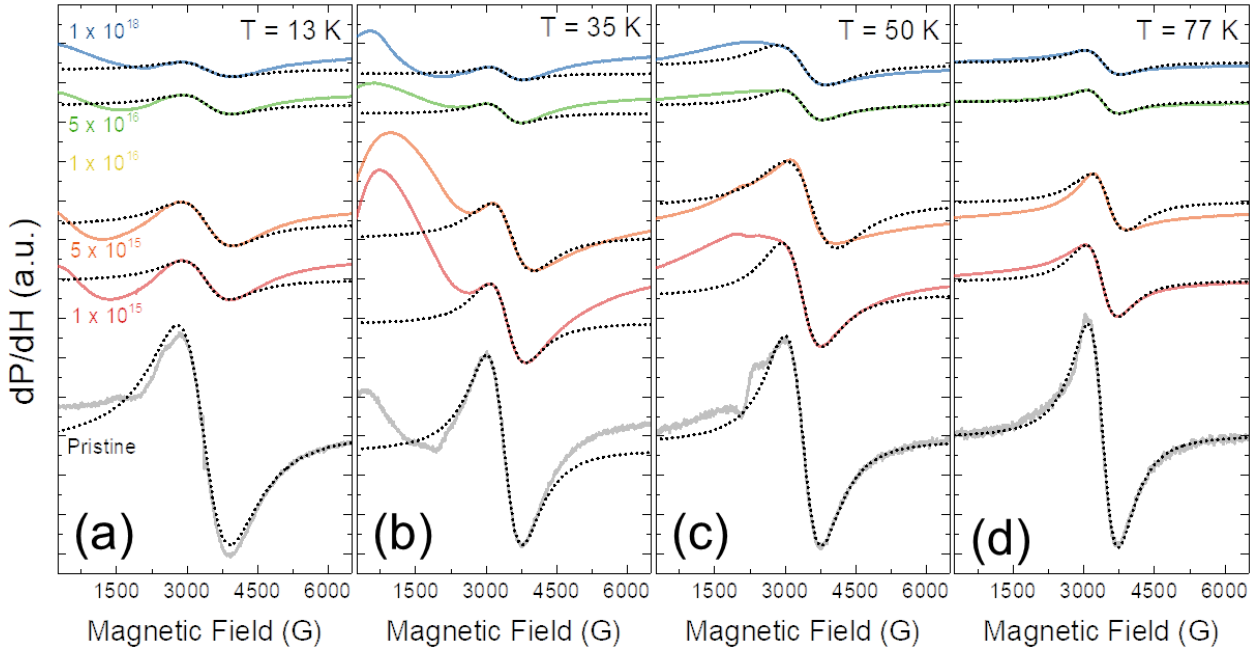

Figure 4.1: EPR spectra as a function of fluence at T = 13 K (a), 35 K (b), 50 K (c) and 77 K (d)

This secondary signal is featured prominently even at 50 K, which is above the T_C. It has been previously reported that two-dimensional ferromagnetic correlations can persist in CST even up to room temperature. [15,25,31] Thus, it is possible that the existence of the secondary signal could be related to these correlations. At 77 K, however, this secondary signal is still present but greatly suppressed, and the spectra across all fluences is dominated by the Cr^{3+} signal.

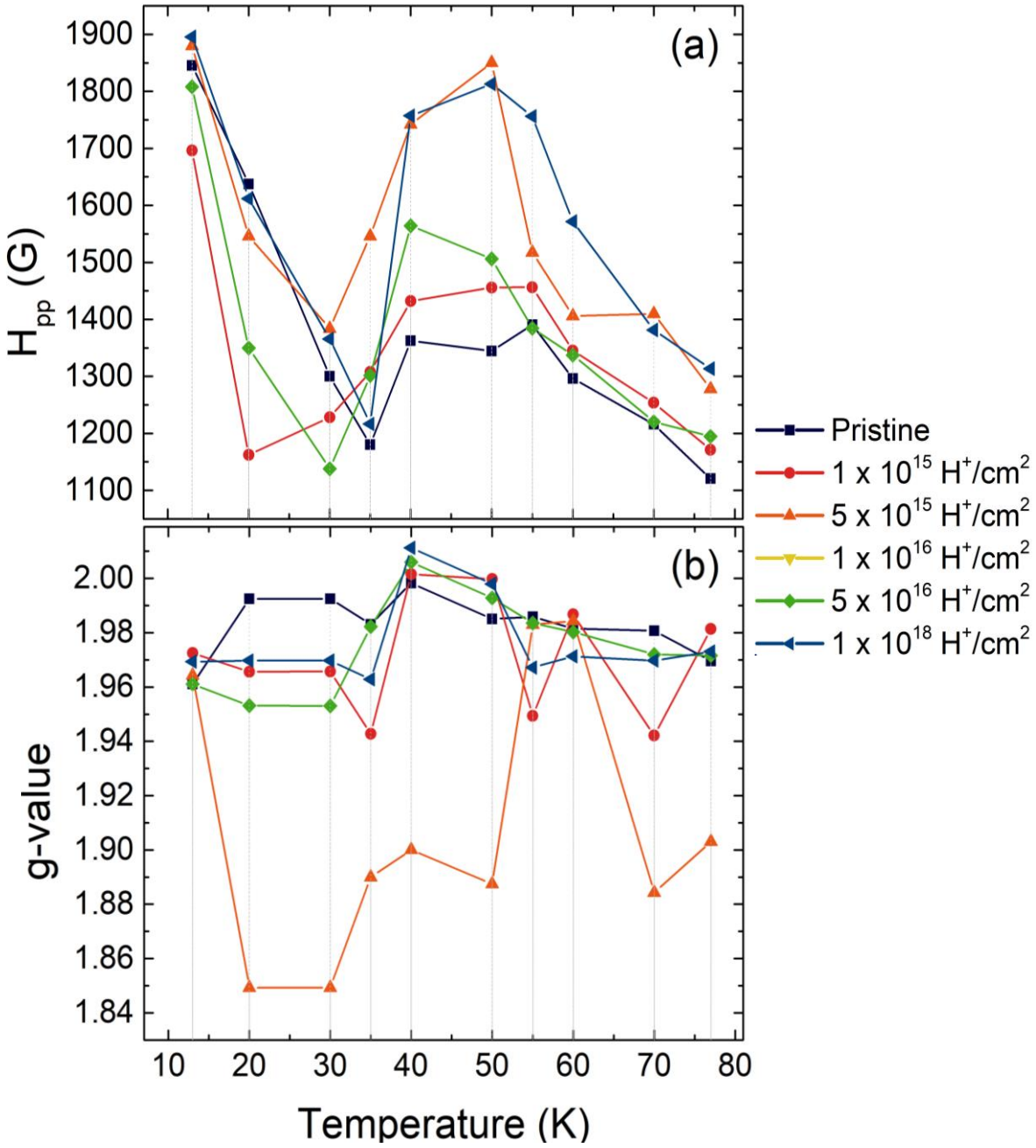

Figure 4.2: Peak-to-peak linewidth H_{pp} (a) and g-value (b) vs. temperature as a function of proton fluence

The temperature dependence of the g-value and peak-to-peak linewidth H_{pp} as a function of fluence was also explored. The temperatures selected correspond with the temperature points from the magnetization vs. magnetic field isotherms. In general, the irradiated compounds show a narrowing of the Cr^{3+} signal below T_C, but in the paramagnetic phase, there is a broadening effect. The g-values for all fluences except 5 x 10^{15} H^+/cm^2 behave similarly in the selected temperature range. Firstly, deviations in g-value from the expected Cr^{3+} value are minimal as the temperature is raised from 13 K. However, at 40 K, there is a significant increase in the g-value for all fluences, with the g-value for some fluences even exceeding 2. This effect is also present in the 5 x 10^{15} H^+/cm^2 fluence, which generally displayed lower g-values than all other fluences below 40 K. It is likely that the fluence and temperature dependent behavior of the EPR spectral parameters is closely related to the behavior of the secondary signal. Moreover, due to its dominance of the spectra, it could affect the accuracy of the Lorentzian fits used to extract the parameters. Therefore, without further experiments, it is difficult to discern the underlying cause behind the observed changes. Regardless, the fluctuations in H_{pp} and g-values and the dominance of the secondary signal in the EPR spectra of the irradiated samples at temperatures below T_C could be an indication of changes to the paramagnetic centers of CST, the local magnetic environments, an emergent secondary magnetic phase, or modifications to the Cr^{3+} - Cr^{3+} superexchange. [34–36]

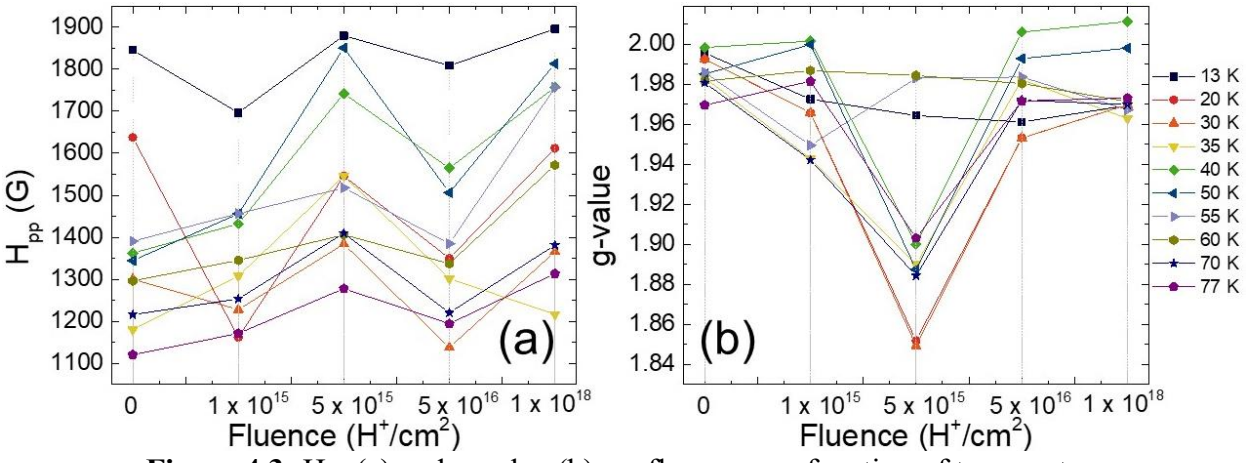

Figure 4.3: H_{pp} (a) and g-value (b) vs. fluence as a function of temperature

CHAPTER 5: CONCLUSIONS AND FUTURE DIRECTIONS

Proton irradiated CST crystals show off the versatility of the magnetic properties of vdW compounds. In this study, crystals irradiated with up to 1 x 10^{18} H^+/cm^2 were studied in a variety of temperature and magnetic field ranges. Through temperature and magnetic field-dependent magnetization, we observe a ferromagnetic phase below $T_C \sim 36$ K for all fluences. Though the T_C remains unchanged after proton irradiation, the saturation magnetization is decreased. Further analysis on the magnetic anisotropy of CST shows a temperature and fluence dependent effect, which could indicate variations in the exchange mechanisms of CST. While further investigations are required, we speculate that the reduced magnetization and uniaxial anisotropy could be a result of reformed short-range intralayer interactions involving the 1st, 2nd, and 3rd nearest neighbor interactions and the interlayer exchange.

Furter evidence of this could be taken from the EPR spectra of the irradiated CST, which show a superposition of two signals. While the expected Cr^{3+} signal is present for all samples, a secondary signal dominates the entire spectra of the samples at varying degrees depending on the temperature and fluence. Although the secondary signal could not be accurately captured by our current experiments, its presence, along with the changes in g-value and linewidth of the Cr^{3+} signal, point to modifications in the magnetic correlations of proton irradiated CST. Overall, the case of proton irradiated CST presents an exciting environment to not only probe the origin of ferromagnetism in CST and other related compounds, but also to explore with methods of tuning their magnetic properties for nanoscale magnetic devices and spintronic applications. In effect, proton irradiation could serve as a fine-tuning knob for the magnetic properties of vdW materials, which is optimal for devices that do not require such dramatic changes as those that will be studied in the following chapters.

PART II: HIGH-TEMPERATURE FERROMAGNETISM VIA ELECTROCHEMICAL INTERCALATION OF ORGANIC MOLECULES

CHAPTER 6: EFFECTS OF INTERCALATION ON VDW SYSTEMS

The versatility of vdW compounds allow for more invasive but still nondestructive methods of magnetic enhancement. There has been much interplay between the magnetic properties of these compounds and their reactions to different dimensionalities, high pressures, proximity effects, and defect engineering. [3–5,37–40] As previously discussed, a viable enhancement method is proton irradiation, which has enhanced the magnetization of FGT and MST. However, for the application of these compounds into consumer applications, a higher T_C is required. Therefore, while the changes brought on by proton irradiation show off the flexibility of these compounds, they are still lacking in terms of high-temperature long-range magnetic ordering. Hence, we look toward intercalation as a more effective enhancement method.

Out of all the compounds studied in this work, bulk FGT presents the highest T_C in its pristine state. [7,29,41,42] Though $T_C \sim 154$ K is still far below room temperature, FGT still holds great potential as a candidate for room temperature ferromagnetism due to its robust chemical and thermal stability. As a layered soft ferromagnet, efforts to increase its T_C have involved the implantation of external molecules between its layers. One report successfully achieved a strong ferromagnetic phase at temperatures above the intrinsic T_C of FGT by sodium intercalation. Though the temperature scale of this investigation was impressive, this phenomenon was caused by decomposition phases that destroyed the crystal structure of FGT and dominated its magnetic ordering, thereby losing the intrinsic properties of the vdW compound. [43] We seek to obtain transformative effects while preserving the vdW character of our compounds by exploring the effects of tetrabutylammonium cation (TBA +) intercalation into their vdW gap.

The intercalation of this organic molecule into $Cr_2Ge_2Te_6$ (CGT) resulted in a dramatically increased T_C and strengthened exchange mechanism without destroying the crystal structure. [44] Indeed, we set out to explore this manageable enhancement method on similar systems and explore

its effects on the magnetization, magnetic anisotropy, and exchange interactions on other ternary transition metal-based chalcogenides. Intercalation was done on CGT, MST, and FGT, which all displayed long-range magnetic ordering (ferromagnetism in CGT and FGT but ferrimagnetism in MST) at temperature above their pristine T_C. As FGT showed a strikingly high T_C value of up to at least 350 K, we focus our investigation on the origin of this effect in FGT through temperature-dependent magnetic anisotropy analysis, Raman spectroscopy, spin-phonon coupling, and theoretical calculations. Our experimental findings continue to prove intercalation as a practical method of engineering high-temperature magnetic devices.

CHAPTER 7: SAMPLE PREPARATION

7.1 Synthesis and Electrochemical Intercalation

The self-flux technique was employed in the growth of $Fe_{2.7}GeTe_2$ crystals as outlined in previous report by Liu and Petrovic. [42] They also provided the $Mn_3Si_2Te_6$ crystals, prepared as outlined in the literature. [45] The resultant millimeter-sized single crystals were intercalated through the process reported by Wang et al. [44] To begin, the crystals are washed with ethanol to remove any possible contaminants. Within a two-electrode cell, the crystals are used as the positive electrode and silver is used as the negative electrode. These two components are submerged in a supersaturated solution of tetrabutylammonium bromide in dimethylformamide, which acts as the electrolyte. The oxidation and reduction processes begin once a constant current is applied, resulting in the intercalation of tetrabutylammonium cations into the crystal vdW gap. The entire process is done in an inert Argon-gas atmosphere. The amount of intercalant can be determined from the resulting discharge curve and specific criteria set by Wang et al.

7.2 Magnetic Characterization

Low temperature bulk magnetometry was conducted using a Quantum Design Physical Property Measurement System with the AC Measurement System option, which provides DC magnetic moment data in a range of 5 K - 350 K in magnetic fields up to 30 kOe. Anisotropic magnetic moment data were collected using a combination of the standard sample holder, Teflon tape, and plastic straw spacers, which minimize any contribution to the sample signal. This setup was used to collect both in-plane and out-of-plane data.

7.3 Supporting Spectroscopy Measurements

7.3.1 Temperature-dependent Raman spectroscopy

Raman spectroscopy measurements were conducted in the parallel polarized configuration for both pristine and intercalated crystals. To minimize any noise in the sample signals, the samples were exfoliated. Measurements were conducted at select temperatures between 3.2 K and 295 K.

7.3.2 X-ray diffraction spectroscopy

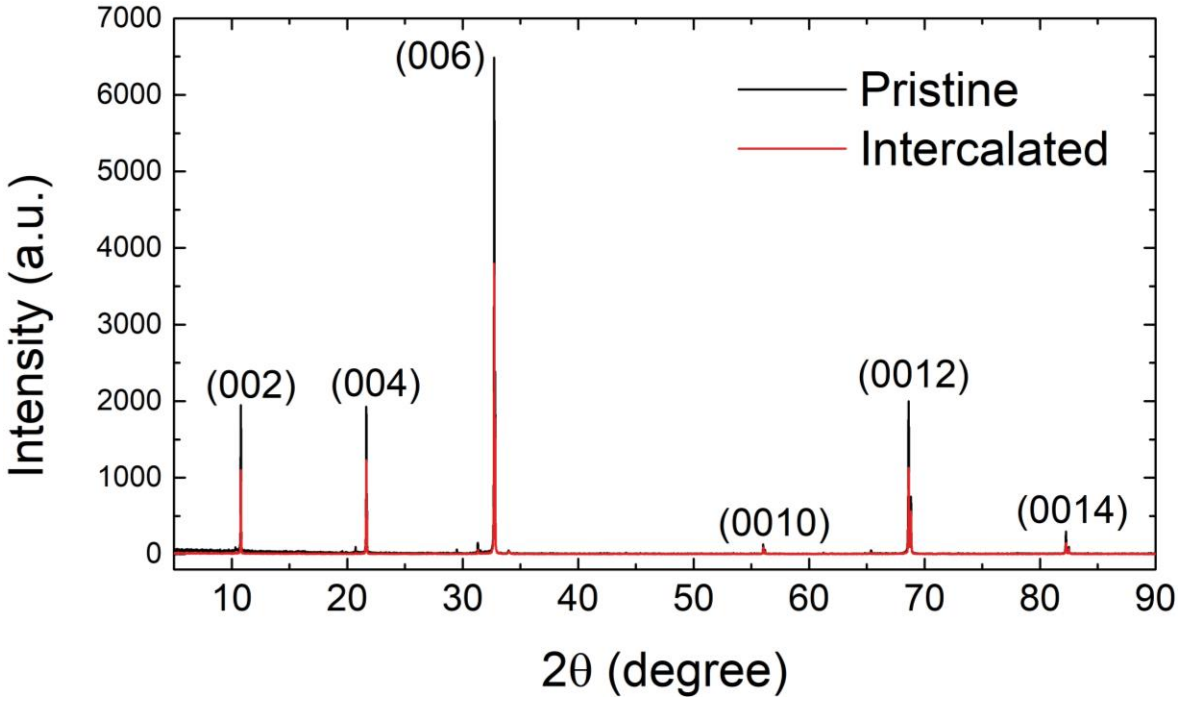

Figure 7.1: Powder x-ray diffraction spectra for both pristine and intercalated FGT

Powder x-ray diffraction data were collected for both pristine and intercalated FGT and are shown in figure 7.1. This data provides assurance that the intercalant molecules indeed occupy the van der Waals gap of the crystal. The destruction of the crystal structure or creation of further lattice defects is of particular concern, as these FGT crystals are Fe-deficient, creating opportunities for the intercalant to damage the crystal and therefore destroy the intrinsic magnetic properties of FGT. From the sharp peaks and correspondence to previous literature, we conclude that the intercalation of TBA+ into FGT did not affect its crystallinity. [29,41,46] Moreover, we

are confident that our observations regarding any changes in the magnetic characteristics of FGT are not a result of crystal structure degradation.

7.4 Theoretical Methods

First-principles simulations were done using the Vienna Ab-initio Simulation Package (VASP) [34], with the PAW pseudo-potentials using the Perdew–Burke–Ernzerhof (PBE) exchange-correlation and an energy cutoff of 600 eV. [47] A 2x2x1 FGT supercell was used to intercalate the TBA+, leading to a supercell containing 154 ions. DFT-D3 corrections accounted for the vdW interactions between the FGT layers and TBA molecules. [48] The relaxations were done using convergence criteria of 10^{-8} eV and a k-mesh of 1x1x1 at the Gamma point. The single-shot calculations were done using convergence criteria of 10^{-9} eV and a k-mesh of 1x1x1 at the Gamma point to compute the charge density. The single-shot calculations were done on the full system (TBA+FGT), and on two subsystems constructed by removing either the FGT or TBA from the full system so that we could compute the charge density difference via $\Delta\rho = \rho(FGT + TBA) - \rho(FGT) - \rho(TBA)$.

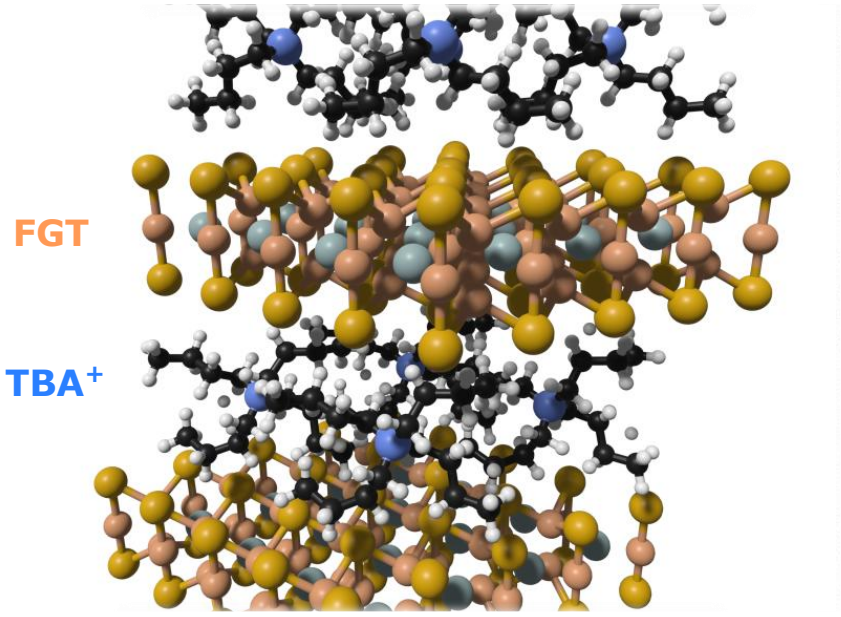

Figure 7.2: Theoretical supercell of FGT intercalated with TBA+

CHAPTER 8: HIGH-TEMPERATURE MAGNETISM AFTER INTERCALATION

Magnetic characterizations were conducted on several vdW chalcogenide systems. The magnetic properties of these compounds are explained as a function of temperature and magnetic field for both intercalated and pristine samples. In the case of FGT and MST, data for the pristine samples were taken from previous reports. [6,7] In all cases, a comparison of intercalated versus pristine does not represent a before-and-after scenario on the same crystal, but rather a case of two separate crystals (one intercalated and the other not) investigated in parallel.

8.1 TEMPERATURE-DEPENDENT MAGNETIZATION

8.1.1 $Mn_3Si_2Te_6$

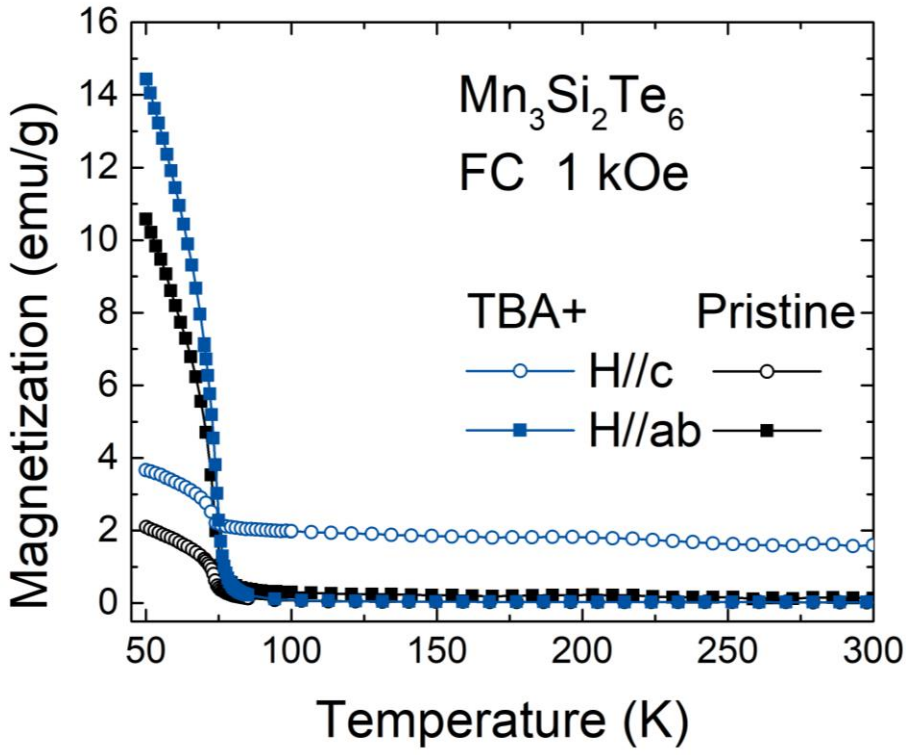

Figure 8.1: Anisotropic field-cooled magnetization vs. temperature for pristine and intercalated MST

Figure 8.1 shows a comparison of the temperature-dependent magnetization of pristine (black) and intercalated (blue) MST. Field cooled (FC) measurements were performed by cooling the sample in the presence of a 1 kOe magnetic field and sweeping the temperature up in

increments. Further information on the anisotropic behavior of MST is acquired by performing the experiment in both the H//ab (open symbols) and the H//c (solid symbols) directions. Firstly, the magnetization is higher for H//ab measurements, confirming an easy-plane magnetization and high magnetocrystalline anisotropy in both samples. At low temperatures, the magnetization of the intercalated MST is noticeably larger than the pristine, showing a nearly two-fold increase along the H//c direction and ~35% increase in the H//ab direction. A sharp transition is estimated to occur at $T_C \sim 72.5$ K by the first derivative of the magnetization with respect to temperature for both pristine and intercalated MST in both directions regardless of cooling field. This transition is well-documented as the transition from ferrimagnetic to paramagnetic states in MST. [6,45] However, in the case of intercalated MST, there is a low but still non-zero H//c magnetization that persists up to the upper limit of 300 K. This is unexpected because the magnetization is expected to be near zero after the transition (see pristine MST for this behavior) due to thermal fluctuations. This high-temperature magnetization may be an indication of a room-temperature ferromagnetic phase induced by intercalation.

8.1.2. $Cr_2Ge_2Te_6$

A similar protocol was followed with intercalated CGT and is shown in figure 8.2. FC measurements (red circles) were done with a cooling field of 500 Oe, which also served as the applied field for the entire measurement. In addition to the FC experiment, we performed zero field cooled (ZFC, in black squares) measurements to observe low field and anisotropic behaviors. ZFC measurements were done by allowing the sample to reach thermal equilibrium at 2 K, and then applying the 500 Oe magnetic field through the temperature sweep. The bifurcation between FC and ZFC measurements in intercalated CGT at low temperatures are a first indication of anisotropic effects. In addition, the measurements were done in both the H//c (solid symbols) and the H//ab (open symbols) orientations for further observation of the anisotropic behavior of CGT.

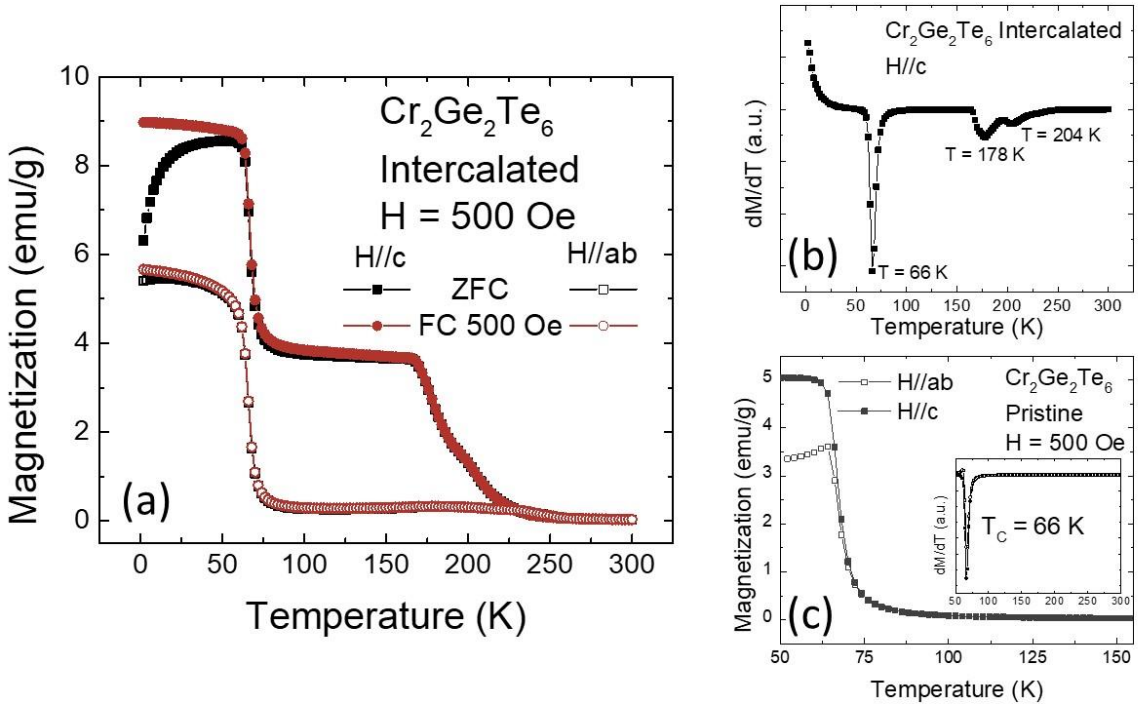

Figure 8.2: Anisotropic magnetization vs. temperature as a function of cooling field (a) for intercalated CGT, dM/dT vs. temperature (b), and pristine magnetization vs. temperature (c) for reference. Inset of (c) is dM/dT vs. temperature of pristine CGT

As expected from the reported magnetocrystalline anisotropy of CGT, the H//c magnetization is higher than the H//ab magnetization at lower fields. A sharp magnetic transition is observed at approximately 66 K, which agrees well with the reported T_C of pristine CGT. [12,14,33] The unexpected behavior of intercalated systems continues with the H//ab magnetization of intercalated CGT, showing a very small but still non-zero magnetization that increases slightly near 200 K before going to zero at 300 K. Most strikingly, the H//c magnetization above 66 K remains relatively high, demonstrating that nearly half the low-temperature magnetization survives the initial transition. This behavior is observed up to approximately 178 K, where another transition begins. The shoulder feature near 204 K may also be a separate magnetic transition, as this temperature agrees well with the reported Curie temperature of intercalated CGT in the study by Wang et al. [44] Again, thermal fluctuations are expected to destabilize the long-range magnetic ordering of pristine CGT above $T_C \sim 66$ K; thus, this non-zero magnetization above 66 K serves as evidence of a possible intermediate ferromagnetic phase caused by intercalation. The behavior of pristine CGT is provided in figure 8.2c to emphasize the effects of intercalation.

8.1.3 $Fe_{2.7}GeTe_2$

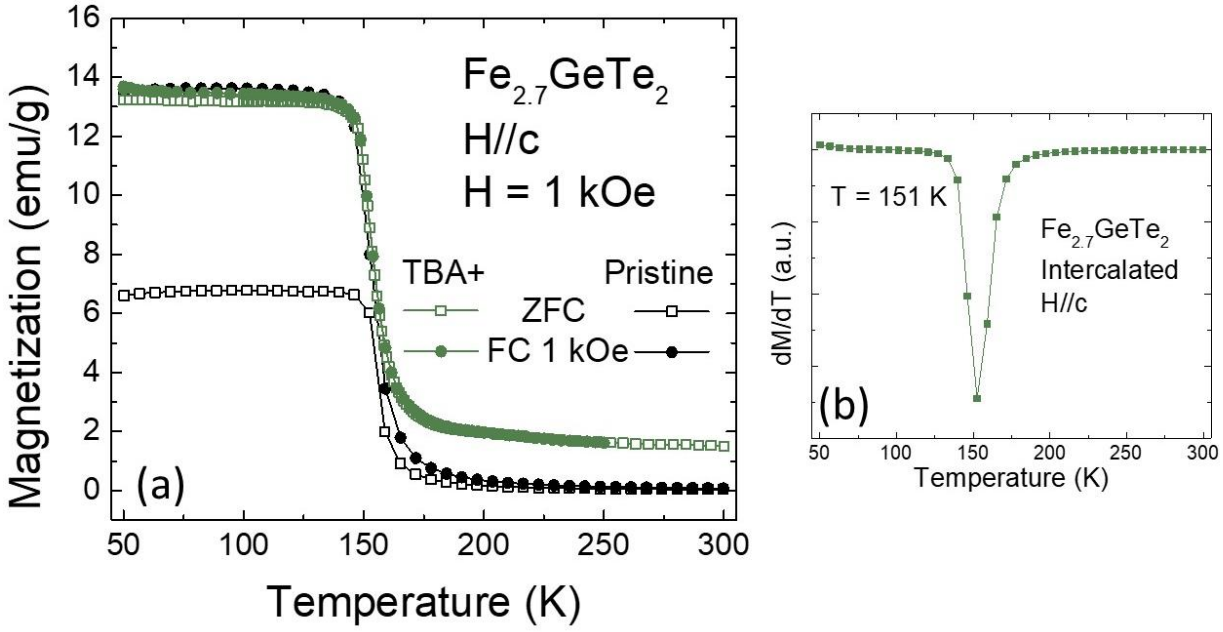

Figure 8.3: Easy-axis magnetization vs. temperature as a function of cooling field for intercalated and pristine FGT (a), dM/dT vs. temperature (b) confirming T_C of intercalated FGT

As in the previous sections, pristine (green) and intercalated (black) FGT were investigated in a temperature range of 50 K – 300 K in figure 8.3a. Both ZFC (open symbols) and FC (solid symbols) measurements were conducted in the H//c direction. Further anisotropic temperature and field-dependent characterization for pristine FGT can be found in previous reports. For ZFC curves, the sample was allowed to stabilize at 50 K before the measuring field of 1 kOe was applied and the temperature was incremented to 300 K. In the case of FC measurements for intercalated FGT, the 1 kOe field was applied during cooling and throughout the temperature sweep to 250 K. Data above 250 K could not be collected due to instrument limitations. ZFC measurements show that a drastic increase in the magnetization of intercalated FGT in comparison to the pristine at low temperatures. While there is not much of a change in the FC response of the intercalated sample, the difference in ZFC magnetization is a first indication that the magnetic character of FGT is altered upon the intercalation of TBA+.

Estimated through the first derivative method in figure 8.3b, we find an initial transition at ~151 K. [7,29,42,43]For FGT, this value agrees well with the reported value of 153 K found in the literature and marks the ferromagnetic to paramagnetic transition temperature. [7,29,41,42] In other words, it appears as though the introduction of TBA+ into the vdW gap of FGT did not completely suppress the intrinsic T_C of FGT. However, for the intercalated sample, this is not a transition into a completely paramagnetic state as there remains a non-zero magnetization that persists at 300 K (explicitly observed in the case of ZFC measurements). Isothermal magnetization data, which is discussed later in this work, will show that this magnetic ordering survives the large number of thermal fluctuations up to at least 350 K. This is atypical of Fe-deficient FGT, as it has been found that decreasing the iron content in FGT leads to lower values of T_C. [49] Considering the initial drop in magnetization at T_C ~ 151 K, we attribute the high-temperature magnetization of FGT to a secondary ferromagnetic phase induced by intercalation with TBA+.

8.2 Hysteresis above intrinsic Curie temperature

The temperature dependent magnetization data serves to introduce the motivation behind taking isothermal magnetization measurements as a function of magnetic field at high temperatures. To prove the existence of long-range ordering above the reported T_C of our samples, we conducted magnetization vs. magnetic field measurements on our intercalated samples in search of a ferromagnetic hysteresis. Samples were cooled to the low temperatures, allowed to reach thermal equilibrium, and subjected to a 5-quadrant magnetic field sweep. After each sweep, the samples were warmed above the intrinsic T_C to avoid any remanent effects from the low temperature phase.

Shown in figure 8.4, intercalated MST (figure 8.4a, 8.4b) and CGT (figure 8.4c, 8.4d) also showed a hysteresis at temperatures far above their reported T_C. In the case of MST, there is "wasp-waisted" hysteresis, the cause of which will be discussed later, along the H//c direction at 100 K (figure 8.4a, blue upright triangles), which exceeds its T_C of ~73 K. This effect is only observed

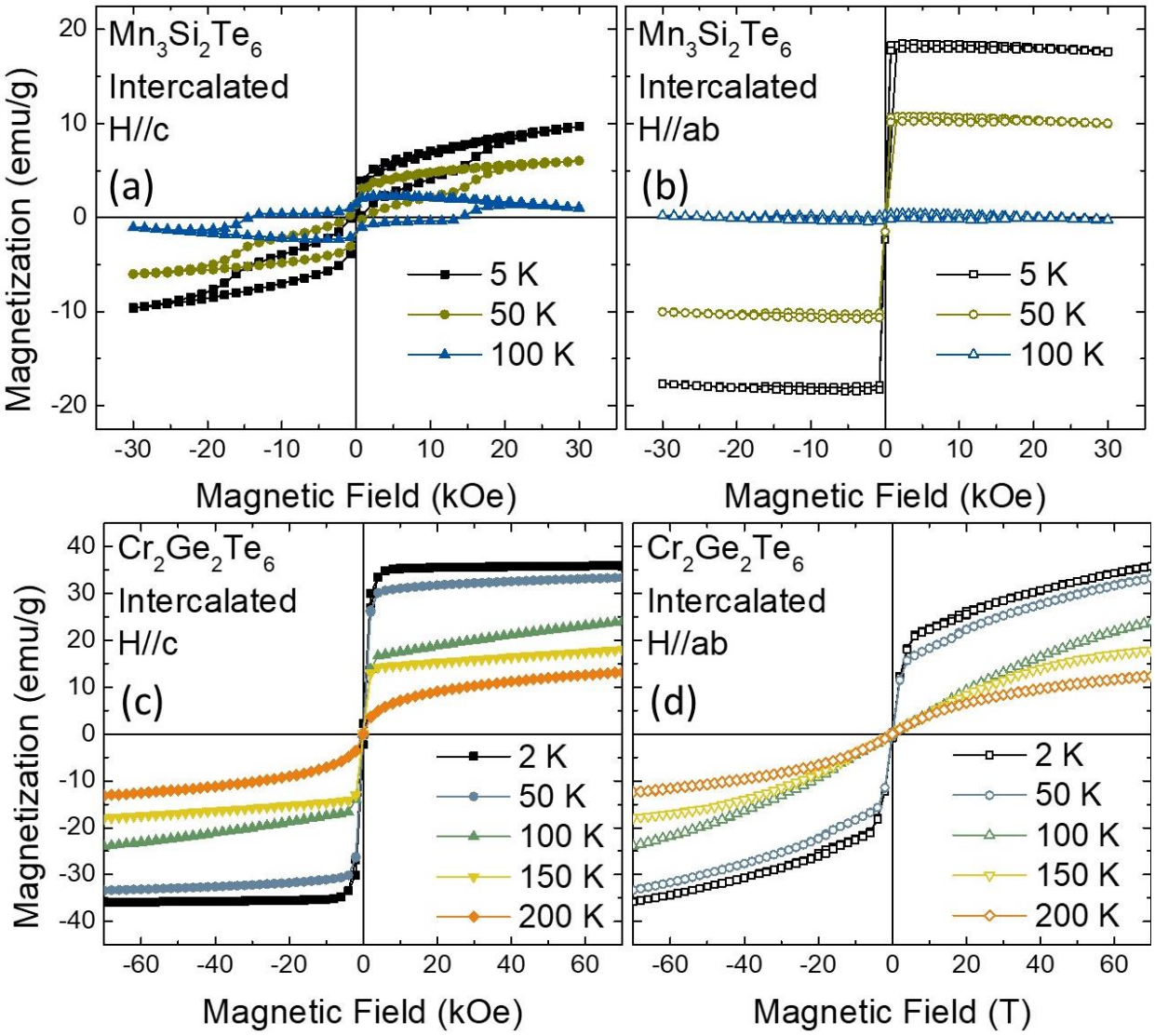

Figure 8.4: H//c (a,c) and H//ab (b,d) magnetization vs. magnetic field as a function of temperature for intercalated MST (a,b) and CGT (c,d)

along the H//c direction, which is odd considering that the easy axis of MST is in the H//ab direction even after intercalation. This is confirmed by the higher H//ab magnetization. However, this H//c magnetization could indicate a possible switching of the magnetic easy axis, which justifies our investigation into the magnetocrystalline anisotropy of these systems. Intercalated CGT exhibits a ferromagnetic hysteresis up to 200 K (figures 8.4c, 8.4d, green upright triangles), far above T_C ~ 66 K. This phenomenon is observed along both the H//c and H//ab direction. In addition, there is an increase in the H//c saturation magnetization of ~50% at 50 K from the pristine value of 20 emu/g. In addition, the H//ab hysteresis curves show a slight kink near 20 kOe, again

calling the anisotropic behavior of intercalated CGT into question. The observation of enhanced thermal stability of the long-range magnetic ordering across different systems shows that the effect should be attributed to the introduction of TBA+. Indeed, the most dramatic effect was observed for FGT, where a wasp-waisted hysteresis was observed at 300 K (figure 8.5a, black squares). This is possible experimental evidence of two coexisting yet competing ferromagnetic phases with vastly different coercivities. [50] Beyond this striking development, magnetic field vs. magnetization measurements taken at the upper limit of our instrument shows that this behavior persists up to 350 K (figure 8.5a, red upright triangle). This marks a drastic increase in the T_C of FGT of over 100% from ~154 K to at least 350 K. Instrumentation limitations did not allow us to find the ferromagnetic to paramagnetic transition temperature for this secondary phase, but the achievement of such enhancement remains notable. At low temperatures, the hysteresis curves demonstrate that the easy axis is still in the H//c direction (figure 8.5b). There is also a kink near 16 kOe, mirroring the behavior of intercalated MST, and strengthening the hypothesis that the novel magnetization behavior is solely due to TBA+ intercalation. Because of the remarkable effects we observed in this compound, the remainder of Part II will focus on our experimental findings regarding the behavior of intercalated FGT.

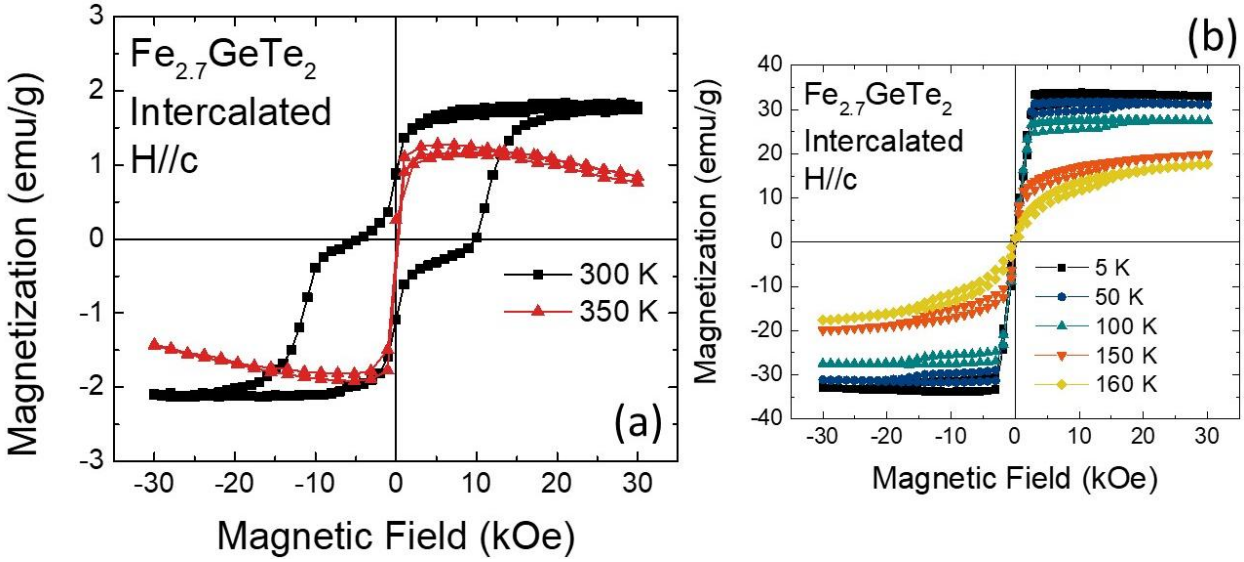

Figure 8.5: H//c magnetization vs. magnetic field as a function of temperature of intercalated FGT at high (a) and low (b) temperatures

CHAPTER 9: RAMAN SPECTROSCOPY

To further investigate the properties of intercalated FGT, we documented its Raman spectra across a range of temperatures ranging from 3.2 K to room temperature. We shifted our focus to two phonon modes, E_{2g}^{2} and A_{1g}^{1} with approximate wavenumbers 125 cm^{-1} and 142 cm^{-1} respectively, which are believed to be sensitive to the magnetic ordering. [51,52] According to those theoretical reports, the E_{2g} and the A_{1g} modes correspond to in-plane vibrations of all constituent atoms and out-of-plane vibrations of Fe and Te atoms respectively. The Goodenough-Kanamori rules present a clear dependence of the magnetic exchange mechanisms of these systems on bond lengths and angles; thus, seeing changes in these modes is of importance. Shown in figure 9.1, the spectra as a function of temperature for both pristine (figure 9.1a) and intercalated (9.1b) FGT are shown, with each phonon mode labeled. Our first observation is a shift in the wavenumber of both modes to lower values after intercalation. [52,53] We attribute this effect to weakened interlayer coupling resulting from increased interlayer distance as the layers are forced apart by the intercalant molecule. More importantly, we also expect this effect from electron doping, as an extra electron per stoichiometric unit is taken into the compound to neutralize the charge of TBA+. In addition, we propose that the observed changes in the magnetic behavior could be correlated to changes in the spin-phonon coupling of our samples. Further analysis incorporates the temperature evolution of the wavenumber for each of the two modes under investigation. Theoretical reports have also observed a discontinuity in the temperature dependence of the wavenumber of these modes near ~150 K, which corresponds to the onset of ferromagnetism of FGT. [51,52] This being the "clear footprint of spin-phonon coupling," as Milosavljević et al. put it, we set to out to experimentally observe and quantify the spin-phonon coupling of FGT before and after intercalation.

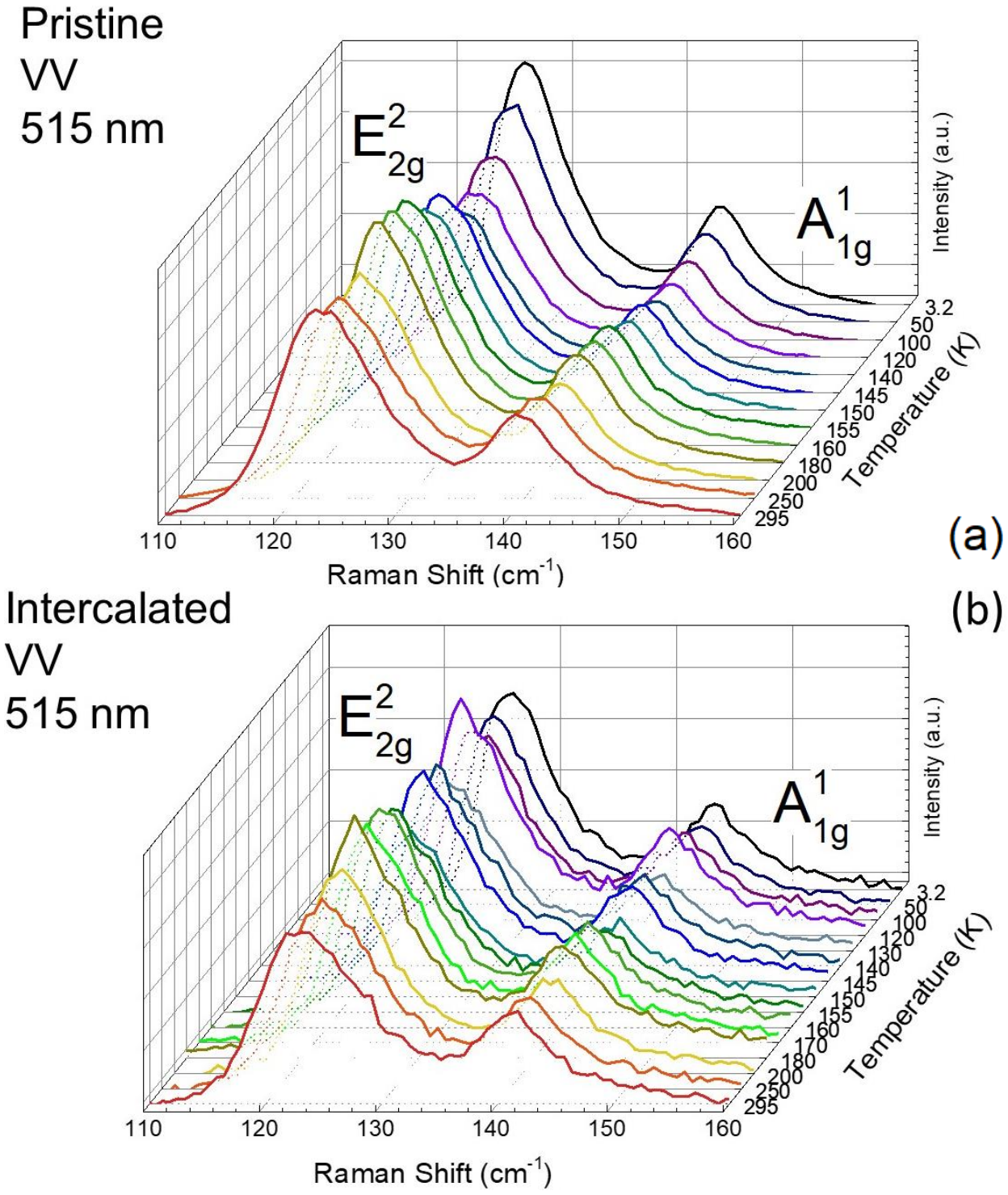

Figure 9.1: Raman spectra for pristine (a) and intercalated (b) FGT as a function of temperature, focused on the E^2_{2g} and A^1_{1g} modes

CHAPTER 10: ANALYSIS AND DISCUSSION

10.1 SPIN-PHONON COUPLING

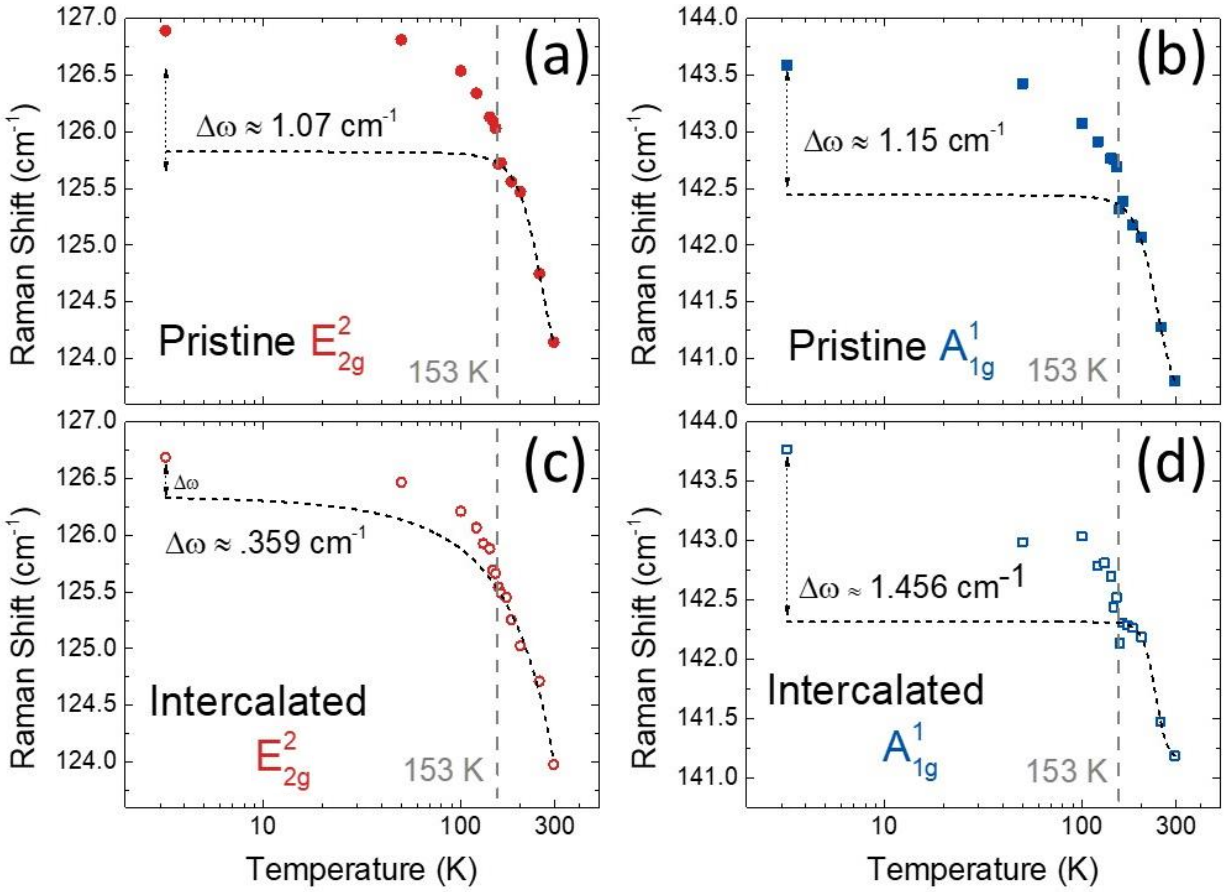

Figure 10.1: Temperature evolution of the Raman shift of both the E_{2g}^2 and A_{1g}^1 modes for pristine (a,b) and intercalated (c,d) FGT. The Boltzmann sigmoidal model is included

Modeling the spectra at each temperature as a superposition of Lorentzian signals (one for each mode), the peak centers (in cm^{-1}) for each mode are plotted with respect to temperature on a logarithmic scale. Evidently, there is a discontinuity in the Raman shift vs. temperature near 153 K, which serves as experimental evidence of spin-phonon coupling. To proceed with the analysis, the points above the intrinsic $T_C \sim 153$ K are fitted with a Boltzmann sigmoidal model. This model simulated the temperature dependent behavior of the Raman shift of each phonon mode. By fitting only the high-temperature points, we extrapolate the low-temperature evolution of the phonon as though it were unperturbed by the magnetic ordering of the system. This process was previously outlined in an investigation of sister compound CST by Casto et al. [25] Like in that report, we

find a clear difference between our experimental data and the simulated behavior below ~153 K. This observation is more evidence of spin-phonon coupling in FGT.

To quantify the spin-phonon coupling across both samples, we extract the difference in wavenumber between the experimental data and the Boltzmann sigmoidal fit. This separation is present at the lowest temperature point recorded experimentally; therefore, we take the separation at 3.2 K between experiment and simulation and denote it as $\Delta\omega$. The spin-phonon coupling parameter λ' is extracted from $\Delta\omega$ through a series of equations and spectroscopic approximations outlined below. Equation 5 presents the relationship between the Raman shift and the spin-phonon coupling, and equation 6 shows a common simplification employed in the extraction of λ'. Equation 7 shows the algebraic extraction of λ'.

$$\omega^2 = \omega_0^2 + \lambda\langle \boldsymbol{S}_i \cdot \boldsymbol{S}_j \rangle \tag{5}$$

$$\omega \approx \omega_0 + \lambda'\langle \boldsymbol{S}_i \cdot \boldsymbol{S}_j \rangle \tag{6}$$

$$\lambda' = \frac{\Delta\omega}{\langle \boldsymbol{S}_i \cdot \boldsymbol{S}_j \rangle} \tag{7}$$

Firstly, ω is the experimental Raman shift (which captures the effects of the spins) and ω_0 represents the Raman shift of the unperturbed mode. Then, $\Delta\omega$ is the difference between these two, which was already extracted in the previous explanation. Then in equation 3, this value is present as the numerator. We assume all the magnetic contribution is coming from the Fe^{3+} cations, which allows us to set the denominator equal to 9/4. This value is chosen as the previous assumption makes $S_i = S_j = 3/2$. From these calculations, we compared the value of λ' for both modes before and after intercalation. The values of λ' are outlined in table 1. These values show that the spin-phonon coupling decreases for the E_{2g}^2 mode, but slightly increase for A_{1g}^1 after intercalation. The presence of spin-phonon coupling is observed for modes involving Fe and Te atoms, which form the key pathway in the dominant magnetic exchange mechanism of FGT. Hence, changes in the spin-phonon coupling could be a result of modifications to the superexchange in FGT stemming from altered metal-ligand bond angles.

Table 10.1: Spin-phonon coupling parameters of pristine and intercalated FGT

		$\Delta\omega$ (cm^{-1})	λ' (cm^{-1})
E_{2g}^2	Pristine	1.07	.476
	Intercalated	.359	.160
A_{1g}^1	Pristine	1.15	.511
	Intercalated	1.456	.647

10.2 Extraction and Analysis of Magnetic Anisotropy Parameters

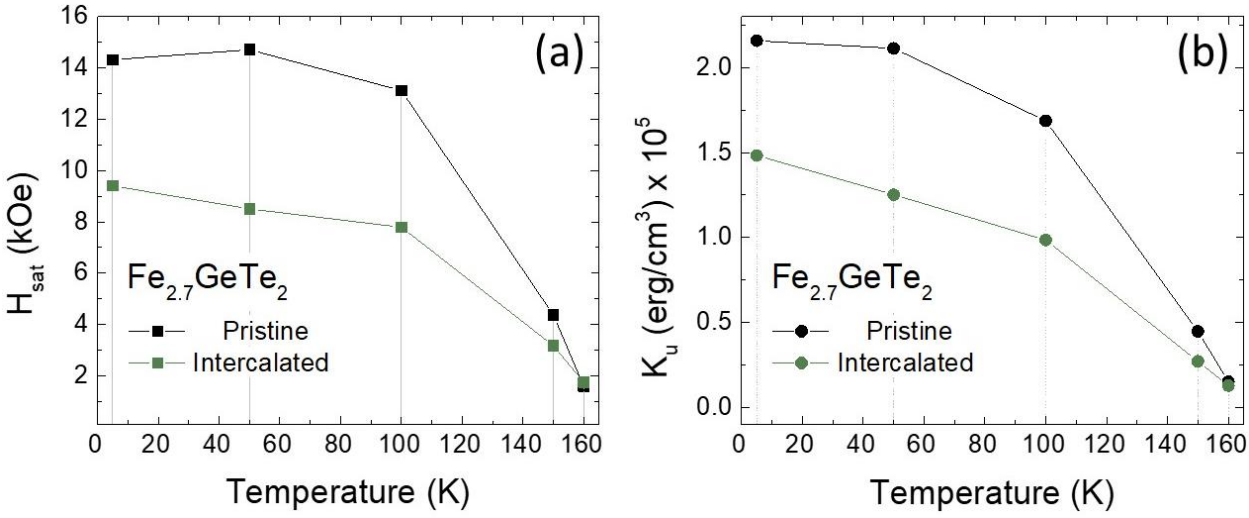

Figure 10.2: Anisotropy field H_{sat} (a) and uniaxial anisotropy constant K_u (b) vs. temperature

Further explanation of the experimentally observed room-temperature ferromagnetic phase may lie in the electronic structure of FGT. In a similar intercalation study on CGT, Wang et al. observed a dramatic increase in T_C caused by the occupation of previously unoccupied d_{xz}/d_{yz} orbitals by the extra electrons introduced into the crystal through intercalation. [44] In that study, the ferromagnetic phase of CGT was substantially strengthened by a shift in the dominant exchange mechanism from a weak superexchange (mediated across the ligand Te atoms like in

FGT) to a much stronger direct exchange between Cr atoms. The Stoner model is commonly used to describe the magnetic ordering of itinerant ferromagnets like FGT. [54–57] Studies on electron-doped FGT have shown that newly introduced electrons begin to occupy d_{xz}/d_{yz} orbitals, which remain unoccupied in pristine FGT. [58,59] This alteration of the electronic density of FGT resulting from electron doping is like that observed by Wang et al. in intercalated CGT. In accordance with the Stoner model, changes in the electronic density of sates near the Fermi level of FGT would result in changes to the ferromagnetic ordering. Hence, we expect that intercalation dopes FGT with electrons and alters the density of states of FGT near the Fermi level which would shift the dominant exchange mechanism from weak superexchange. A strong Fe-Fe direct exchange (like the Cr-Cr direct exchange observed in intercalated CGT) would be facilitated by intercalation and stabilize the ferromagnetism at high temperatures.

The change in the electronic density of states in CGT also resulted in a complete magnetic easy axis switch from out-of-plane to in-plane as the new electrons introduced a planar orbital moment. [44] While our experimental data did not show such drastic changes, we present evidence that the anisotropy of intercalated FGT is decreased in comparison to its pristine counterpart. This lends strength to the possibility of changes in the exchange mechanism via intercalation-induced electron doping in our sample. Indeed, intercalated FGT shows a lower saturation field along the H//ab than pristine FGT (figure 10.2a), which indicates that it takes less energy to overcome the anisotropy energy barrier and align the moments along the hard axis. The uniaxial anisotropy constants K_u are estimated through the Stoner-Wohlfarth model. These parameters are related to the saturation magnetization M_s in equation 4. The change in anisotropy can be more readily attributed to the decrease in anisotropy field rather than a decrease in magnetization. Moreover, K_u is consistently lower for the intercalated FGT throughout the lower temperature regime, again confirming a decreased anisotropy after intercalation (figure 10.2b). In theoretical studies of electron doped FGT, contributions from previously unoccupied d_{xz}/d_{yz} orbitals served as mediators for change in the anisotropy energy without significantly altering the magnetic moment per Fe atom. [58] Our experimental data shows a clear reduction in anisotropy, but no appreciable

changes in the magnetization. Therefore, it is possible the electrons introduced through intercalation may occupy these previously unoccupied states, which would give rise to similar behavior observed in intercalated CGT. If this is the case, then our experimental evidence of reduced magnetic anisotropy may be an indirect observation unoccupied d_{xz}/d_{yz} orbital occupation and subsequent shift in the exchange mechanism from a relatively weak superexchange to a stronger direct exchange that allows the ferromagnetism to survive up to 350 K.

CHAPTER 11: THEORETICAL EVIDENCE OF CHARGE TRANSFER EFFECT

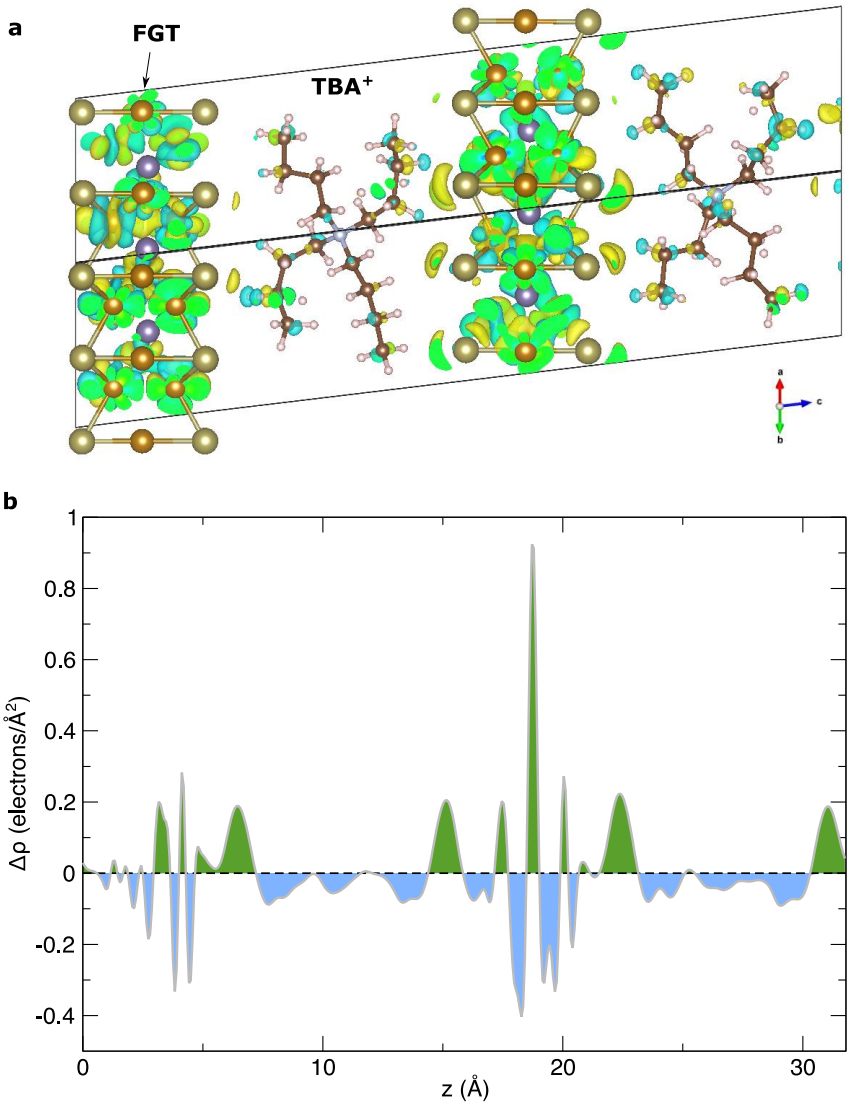

Figure 11.1: Charge density difference ($\Delta\rho = \rho(\mathrm{FGT + TBA}) - \rho(\mathrm{FGT}) - \rho(\mathrm{TBA})$, where $\rho(\mathrm{FGT + TBA})$ is the total charge density of FGT plus TBA, $\rho(\mathrm{FGT})$ is the charge density of the isolated FGT system, and $\rho(\mathrm{TBA})$ is the charge density of the TBA

Theoretical first principles calculations allowed us to confirm the presence of a charge reorganization effect. The calculations provide a picture of the charge density difference between the intercalated FGT and its constituents. In other words, the charge densities of isolated FGT and TBA+ are subtracted from the charge density of the intercalated FGT, which includes contributions from both FGT and TBA+. The results are visualized in figure and show that the electrons of TBA+ contribute to a large change in the charge density around the Fe and Te atoms of the

simulated FGT layer. Moreover, there appears to be no change in the charge density of the Ge atoms. This charge transfer effect also explains the shift in wavenumber of the Raman modes under investigation in Chapter 9. Overall, because the charge transfer effect is contained to mainly Fe and Te atoms, it is likely that it has substantial implications on the exchange mechanisms of FGT.

CHAPTER 12: CONCLUSION AND FUTURE DIRECTIONS

In summary, tetrabutylammonium cations were electrochemically inserted between the layers of FGT, CGT, and MST bulk crystals. The effects of intercalation on the magnetic properties of these systems were investigated through temperature and magnetic field-dependent magnetization measurements, x-ray diffraction and temperature-dependent Raman spectroscopy, and theoretical calculations. Our findings revealed a significant magnetization above the intrinsic T_C of each compound, indicating a high-temperature long-range magnetic ordering, which we attribute to the introduction of TBA+ to the vdW gap of the crystals. Most drastically, FGT showed ferromagnetic characteristics up to 350 K without suppressing the initial transition at ~151 K or significant changes to the bulk magnetization. Moreover, the layered structure of FGT was unaffected. Hence, we shifted our focus to FGT.

Temperature-dependent Raman measurements provided clear experimental evidence of spin-phonon coupling in FGT and an electron doping effect. Theoretical calculations also suggest that a charge transfer effect could be the reason for the high temperature ferromagnetism. These findings could also be evidence of changes to the dominant exchange mechanism in FGT. In effect, our study on intercalated transition metal-based vdW chalcogenides presents a compelling case for intercalation as a non-destructive and feasible technique of creating room-temperature magnetic devices to be incorporated into consumer applications.

In essence, these two experiments have proved that vdW magnets allow for versatile of their magnetic character through non-destructive methods. We hypothesize that modified exchange mechanisms could be behind the observed changes. Ideally this could create a landscape where specific exchange mechanisms are targeted and enhanced based on their usefulness for different purposes. More experiments are needed to pinpoint the exact processes within this work. Refining our EPR measurement procedures to accurately capture the evolution of the observed secondary signal would be helpful in further deciphering the magnetic correlations in irradiated CST. We also propose varying the energy of the proton beam to make connections between

magnetic properties and the energy of the incident protons on the crystal. Neutron diffraction measurements could help reveal the short-range interactions that have changed upon irradiation or intercalation. In the case of intercalation, we were unable to capture the upper thermal threshold of the high-temperature long-range magnetic ordering for intercalated MST and FGT; therefore, we need to expand the temperature and magnetic field range used when characterizing these systems. Overall, this work is still in progress, but both intercalation and proton irradiation are good techniques for not only adapting vdW magnets to our favor, but also for expanding our fundamental understanding of their inner workings.

REFERENCES

[1] Q. H. Wang et al., *The Magnetic Genome of Two-Dimensional van Der Waals Materials*, ACS Nano (2022).

[2] H. Li, S. Ruan, and Y.-J. Zeng, *Intrinsic Van Der Waals Magnetic Materials from Bulk to the 2D Limit: New Frontiers of Spintronics*, Advanced Materials **31**, 1900065 (2019).

[3] X. Jiang, Q. Liu, J. Xing, N. Liu, Y. Guo, Z. Liu, and J. Zhao, *Recent Progress on 2D Magnets: Fundamental Mechanism, Structural Design and Modification*, Applied Physics Reviews **8**, 031305 (2021).

[4] K. F. Mak, J. Shan, and D. C. Ralph, *Probing and Controlling Magnetic States in 2D Layered Magnetic Materials*, Nat Rev Phys **1**, 646 (2019).

[5] J.-F. Dayen, S. J. Ray, O. Karis, I. J. Vera-Marun, and M. V. Kamalakar, *Two-Dimensional van Der Waals Spinterfaces and Magnetic-Interfaces*, Applied Physics Reviews **7**, 011303 (2020).

[6] L. M. Martinez, H. Iturriaga, R. Olmos, L. Shao, Y. Liu, T. T. Mai, C. Petrovic, A. R. Hight Walker, and S. R. Singamaneni, *Enhanced Magnetization in Proton Irradiated Mn3Si2Te6 van Der Waals Crystals*, Appl. Phys. Lett. **116**, 172404 (2020).

[7] R. Olmos, A. Cosio, C. L. Saiz, L. M. Martinez, L. Shao, Q. Wang, and S. R. Singamaneni, *Magnetic Properties of Proton Irradiated Fe2.7GeTe2 Bulk Crystals*, MRS Advances **4**, 2185 (2019).

[8] T. Shi, Q. Peng, Z. Bai, F. Gao, and I. Jovanovic, *Proton Irradiation of Graphene: Insights from Atomistic Modeling*, Nanoscale **11**, 20754 (2019).

[9] O. V. Yazyev, *Magnetism in Disordered Graphene and Irradiated Graphite*, Phys. Rev. Lett. **101**, 037203 (2008).

[10] M.-W. Lin et al., *Ultrathin Nanosheets of CrSiTe3: A Semiconducting Two-Dimensional Ferromagnetic Material*, J. Mater. Chem. C **4**, 315 (2015).

[11] B. Huang et al., *Layer-Dependent Ferromagnetism in a van Der Waals Crystal down to the Monolayer Limit*, Nature **546**, 7657 (2017).

[12] Y. Liu and C. Petrovic, *Anisotropic Magnetic Entropy Change in Cr2X2Te6 (X = Si and Ge)*, Phys. Rev. Materials **3**, 014001 (2019).

[13] V. Carteaux, G. Ouvrard, J. C. Grenier, and Y. Laligant, *Magnetic Structure of the New Layered Ferromagnetic Chromium Hexatellurosilicate Cr2Si2Te6*, Journal of Magnetism and Magnetic Materials **94**, 127 (1991).

[14] B. Siberchicot, S. Jobic, V. Carteaux, P. Gressier, and G. Ouvrard, *Band Structure Calculations of Ferromagnetic Chromium Tellurides CrSiTe3 and CrGeTe3*, J. Phys. Chem. **100**, 5863 (1996).

[15] B. Liu, Y. Zou, L. Zhang, S. Zhou, Z. Wang, W. Wang, Z. Qu, and Y. Zhang, *Critical Behavior of the Quasi-Two-Dimensional Semiconducting Ferromagnet CrSiTe3*, Sci Rep **6**, 1 (2016).

[16] W. Niu, X. Zhang, W. Wang, J. Sun, Y. Xu, L. He, W. Liu, and Y. Pu, *Probing the Atomic-Scale Ferromagnetism in van Der Waals Magnet $CrSiTe_3$*, Appl. Phys. Lett. **119**, 172402 (2021).

[17] R. Olmos, J. A. Delgado, H. Iturriaga, L. M. Martinez, C. L. Saiz, L. Shao, Y. Liu, C. Petrovic, and S. R. Singamaneni, *Critical Phenomena of the Layered Ferrimagnet Mn3Si2Te6 Following Proton Irradiation*, Journal of Applied Physics **130**, 013902 (2021).

[18] A. F. May, Y. Liu, S. Calder, D. S. Parker, T. Pandey, E. Cakmak, H. Cao, J. Yan, and M. A. McGuire, *Magnetic Order and Interactions in Ferrimagnetic Mn3Si2Te6*, Phys. Rev. B **95**, 174440 (2017).

[19] E. Gamsjäger and M. Wiessner, *Low Temperature Heat Capacities and Thermodynamic Functions Described by Debye–Einstein Integrals*, Monatsh Chem **149**, 357 (2018).

[20] A. F. May, Y. Liu, S. Calder, D. S. Parker, T. Pandey, E. Cakmak, H. Cao, J. Yan, and M. A. McGuire, *Magnetic Order and Interactions in Ferrimagnetic Mn3Si2Te6*, Phys. Rev. B **95**, 174440 (2017).

[21] H. Nhalil et al., *Antiferromagnetism and the Emergence of Frustration in the Sawtooth Lattice Chalcogenide Olivines Mn2SiS4−xSex (x = 0–4)*, Phys. Rev. B **99**, 184434 (2019).

[22] A. Junod, K.-Q. Wang, G. Triscone, and G. Lamarche, *Specific Heat, Magnetic Properties and Critical Behaviour of Mn2SiS4 and Fe2GeS4*, Journal of Magnetism and Magnetic Materials **146**, 21 (1995).

[23] P. A. Joy and S. Vasudevan, *Magnetism in the Layered Transition-Metal Thiophosphates MPS3 (M=Mn, Fe, and Ni)*, Phys. Rev. B **46**, 5425 (1992).

[24] Y. Takano, N. Arai, A. Arai, Y. Takahashi, K. Takase, and K. Sekizawa, *Magnetic Properties and Specific Heat of MPS3 (M=Mn, Fe, Zn)*, Journal of Magnetism and Magnetic Materials **272–276**, E593 (2004).

[25] L. D. Casto et al., *Strong Spin-Lattice Coupling in CrSiTe3*, APL Materials **3**, 041515 (2015).

[26] *A Mechanism of Magnetic Hysteresis in Heterogeneous Alloys*, https://doi.org/10.1098/rsta.1948.0007.

[27] C. Zhang et al., *Hard Ferromagnetic Behavior in Atomically Thin $CrSiTe_3$ Flakes*, Nanoscale **14**, 5851 (2022).

[28] N. Richter, D. Weber, F. Martin, N. Singh, U. Schwingenschlögl, B. V. Lotsch, and M. Kläui, *Temperature-Dependent Magnetic Anisotropy in the Layered Magnetic Semiconductors CrI3 and CrBr3*, Phys. Rev. Materials **2**, 024004 (2018).

[29] Y. Liu, J. Li, J. Tao, Y. Zhu, and C. Petrovic, *Anisotropic Magnetocaloric Effect in Fe3−xGeTe2*, Sci Rep **9**, 13233 (2019).

[30] J. Zhang et al., *Unveiling Electronic Correlation and the Ferromagnetic Superexchange Mechanism in the van Der Waals Crystal CrSiTe3*, Phys. Rev. Lett. **123**, 047203 (2019).

[31] T. J. Williams, A. A. Aczel, M. D. Lumsden, S. E. Nagler, M. B. Stone, J.-Q. Yan, and D. Mandrus, *Magnetic Correlations in the Quasi-Two-Dimensional Semiconducting Ferromagnet CrSiTe3*, Phys. Rev. B **92**, 144404 (2015).

[32] N. Sivadas, M. W. Daniels, R. H. Swendsen, S. Okamoto, and D. Xiao, *Magnetic Ground State of Semiconducting Transition-Metal Trichalcogenide Monolayers*, Phys. Rev. B **91**, 235425 (2015).

[33] D.-H. Kim, K. Kim, K.-T. Ko, J. Seo, J. S. Kim, T.-H. Jang, Y. Kim, J.-Y. Kim, S.-W. Cheong, and J.-H. Park, *Giant Magnetic Anisotropy Induced by Ligand L S Coupling in Layered Cr Compounds*, Phys. Rev. Lett. **122**, 207201 (2019).

[34] C. L. Saiz, M. A. McGuire, S. R. J. Hennadige, J. van Tol, and S. R. Singamaneni, *Electron Spin Resonance Properties of CrI3 and CrCl3 Single Crystals*, MRS Advances **4**, 2169 (2019).

[35] S. R. Singamaneni, L. M. Martinez, J. Niklas, O. G. Poluektov, R. Yadav, M. Pizzochero, O. V. Yazyev, and M. A. McGuire, *Light Induced Electron Spin Resonance Properties of van Der Waals CrX3 (X = Cl, I) Crystals*, Appl. Phys. Lett. **117**, 082406 (2020).

[36] W. Bai et al., *Parasitic Ferromagnetism in Few-Layered Transition-Metal Chalcogenophosphate*, J. Am. Chem. Soc. **142**, 10849 (2020).

[37] Z. Wang, D. Sapkota, T. Taniguchi, K. Watanabe, D. Mandrus, and A. F. Morpurgo, *Tunneling Spin Valves Based on Fe3GeTe2/HBN/Fe3GeTe2 van Der Waals Heterostructures*, Nano Lett. **18**, 4303 (2018).

[38] Y. Wang and J. Yi, *Chapter 4 - Ferromagnetism in Two-Dimensional Materials via Doping and Defect Engineering*, in *Spintronic 2D Materials*, edited by W. Liu and Y. Xu (Elsevier, 2020), pp. 95–124.

[39] Y. Sun, R. Wang, and K. Liu, *Substrate Induced Changes in Atomically Thin 2-Dimensional Semiconductors: Fundamentals, Engineering, and Applications*, Applied Physics Reviews **4**, 011301 (2017).

[40] X. Hu, Y. Zhao, X. Shen, A. V. Krasheninnikov, Z. Chen, and L. Sun, *Enhanced Ferromagnetism and Tunable Magnetism in Fe3GeTe2 Monolayer by Strain Engineering*, ACS Appl. Mater. Interfaces **12**, 26367 (2020).

[41] A. F. May, S. Calder, C. Cantoni, H. Cao, and M. A. McGuire, *Magnetic Structure and Phase Stability of the van Der Waals Bonded Ferromagnet Fe3-xGeTe2*, Phys. Rev. B **93**, 014411 (2016).

[42] Y. Liu, V. N. Ivanovski, and C. Petrovic, *Critical Behavior of the van Der Waals Bonded Ferromagnet Fe3-xGeTe2*, Phys. Rev. B **96**, 144429 (2017).

[43] D. Weber, A. H. Trout, D. W. McComb, and J. E. Goldberger, *Decomposition-Induced Room-Temperature Magnetism of the Na-Intercalated Layered Ferromagnet Fe3–XGeTe2*, Nano Lett. **19**, 5031 (2019).

[44] N. Wang et al., *Transition from Ferromagnetic Semiconductor to Ferromagnetic Metal with Enhanced Curie Temperature in Cr2Ge2Te6 via Organic Ion Intercalation*, J. Am. Chem. Soc. **141**, 17166 (2019).

[45] Y. Liu and C. Petrovic, *Critical Behavior and Magnetocaloric Effect in Mn3si2Te6*, Phys. Rev. B **98**, 064423 (2018).

[46] S. Liu et al., *Wafer-Scale Two-Dimensional Ferromagnetic Fe3GeTe2 Thin Films Grown by Molecular Beam Epitaxy*, Npj 2D Mater Appl **1**, 30 (2017).

[47] G. Kresse and J. Furthmüller, *Efficient Iterative Schemes for Ab Initio Total-Energy Calculations Using a Plane-Wave Basis Set*, Phys. Rev. B **54**, 11169 (1996).

[48] S. Grimme, J. Antony, S. Ehrlich, and H. Krieg, *A Consistent and Accurate Ab Initio Parametrization of Density Functional Dispersion Correction (DFT-D) for the 94 Elements H-Pu*, J. Chem. Phys. **132**, 154104 (2010).

[49] A. F. May, D. Ovchinnikov, Q. Zheng, R. Hermann, S. Calder, B. Huang, Z. Fei, Y. Liu, X. Xu, and M. A. McGuire, *Ferromagnetism Near Room Temperature in the Cleavable van Der Waals Crystal Fe5GeTe2*, ACS Nano **13**, 4436 (2019).

[50] L. H. Bennett and E. Della Torre, *Analysis of Wasp-Waist Hysteresis Loops*, Journal of Applied Physics **97**, 10E502 (2005).

[51] A. Milosavljević, A. Šolajić, S. Djurdjić-Mijin, J. Pešić, B. Višić, Y. Liu, C. Petrovic, N. Lazarević, and Z. V. Popović, *Lattice Dynamics and Phase Transitions in Fe3−xGeTe2*, Phys. Rev. B **99**, 214304 (2019).

[52] X. Kong, T. Berlijn, and L. Liang, *Thickness and Spin Dependence of Raman Modes in Magnetic Layered Fe3GeTe2*, Advanced Electronic Materials **7**, 2001159 (2021).

[53] J. Yan, Y. Zhang, P. Kim, and A. Pinczuk, *Electric Field Effect Tuning of Electron-Phonon Coupling in Graphene*, Phys. Rev. Lett. **98**, 166802 (2007).

[54] H. L. Zhuang, P. R. C. Kent, and R. G. Hennig, *Strong Anisotropy and Magnetostriction in the Two-Dimensional Stoner Ferromagnet Fe3GeTe2*, Phys. Rev. B **93**, 134407 (2016).

[55] B. Chen, J. Yang, H. Wang, M. Imai, H. Ohta, C. Michioka, K. Yoshimura, and M. Fang, *Magnetic Properties of Layered Itinerant Electron Ferromagnet Fe_3GeTe_2*, J. Phys. Soc. Jpn. **82**, 124711 (2013).

[56] N. León-Brito, E. D. Bauer, F. Ronning, J. D. Thompson, and R. Movshovich, *Magnetic Microstructure and Magnetic Properties of Uniaxial Itinerant Ferromagnet Fe3GeTe2*, J. Appl. Phys. **120**, 083903 (2016).

[57] C. Tan, J. Lee, S.-G. Jung, T. Park, S. Albarakati, J. Partridge, M. R. Field, D. G. McCulloch, L. Wang, and C. Lee, *Hard Magnetic Properties in Nanoflake van Der Waals Fe3GeTe2*, Nat Commun **9**, 1554 (2018).

[58] Y. Deng et al., *Gate-Tunable Room-Temperature Ferromagnetism in Two-Dimensional Fe3GeTe2*, Nature **563**, 94 (2018).

[59] X. Huang, J. Xu, R. Zeng, Q. Jiang, X. Nie, C. Chen, X. Jiang, and J.-M. Liu, *Li-Ion Intercalation Enhanced Ferromagnetism in van Der Waals Fe_3GeTe_2 Bilayer*, Appl. Phys. Lett. **119**, 012405 (2021).

VITA

My name is Hector Iturriaga, and I began my academic career with the 2016 UTEP Honor's Convocation at the start of my Bachelor of Science degree in Physics. In 2018, I was hired as an undergraduate teaching assistant and had the privilege to teach introductory mechanics to other young physicists and engineers. During a timely TA shortage, I met Dr. Srinivasa Rao Singamaneni and while I initially went into his office for some scantrons, I ultimately came out with an offer for a Nuclear Regulatory Commission undergraduate research fellowship. Under this program, I completed my undergraduate degree in May of 2020 with highest honors.

Since early 2019, I've had the privilege of presenting or submitting work to several conferences like Materials Research Society meetings, contributing towards peer-reviewed publications, and preparing two of my own. As part of Dr. Singamaneni's group, I also had the opportunity to work in Ames Laboratory, a federally funded national lab, on two separate occasions through both the UT System Louis-Stokes Alliance for Minority Participation program and the Department of Energy. I am forever grateful for my time spent in the Nanomagnetic Materials Lab as it has prepared me to successfully compete for several honors such as UTEP graduate school funding awards, scholarships, departmental and college of science academic and research accolades, support from the NSF GRFP, opportunities from the National Nuclear Security Administration, and admission into some of the nation's top doctoral programs.

Contact Information: hiturriaga3@gmail.com